Geophysical Journal International

Geophys. J. Int. (2015) **203,** 1436–1459 doi: 10.1093/gji/ggv365
GJI Geodynamics and tectonics

Seismogenic faulting of the sedimentary sequence and laterally variable material properties in the Zagros Mountains (Iran) revealed by the August 2014 Murmuri (E. Dehloran) earthquake sequence

Alex Copley,[1] Ezgi Karasozen,[2] Behnam Oveisi,[3] John R. Elliott,[4] Sergey Samsonov[5] and Edwin Nissen[2]

[1] *COMET, Bullard Labs, Department of Earth Sciences, University of Cambridge, Cambridge, United Kingdom. E-mail: acc41@cam.ac.uk*
[2] *Colorado School of Mines, Golden, CO, USA*
[3] *Seismotectonics Department, Geological Survey of Iran, Azadi Square, Meraj Blvd, Tehran, Iran*
[4] *COMET, Department of Earth Sciences, University of Oxford, Oxford, United Kingdom*
[5] *Canada Centre for Mapping and Earth Observation, Natural Resources Canada, Ottawa, Canada*

Accepted 2015 September 2. Received 2015 August 20; in original form 2015 May 15

SUMMARY

We present source models for the August 2014 Murmuri (Dehloran) earthquake sequence in the Zagros Mountains of Iran. An M_w6.2 mainshock was followed by an aftershock sequence containing five events of $M_w \geq 5.4$. Models of *P* and *SH* waveforms show that all events had dominantly thrust-faulting mechanisms, and had centroid depths that place them within the thick sedimentary sequence, above the crystalline basement. The combination of our estimated focal mechanisms, relative relocations of the event hypocentres and the surface displacement patterns observed using InSAR imply that the mainshock and largest aftershock ruptured different fault planes and both contributed to the surface deformation. The fault planes both slipped in horizontally elongated patches, possibly due to rheological layering limiting the updip and downdip extent of rupture. The slip vector of the Murmuri mainshock implies that the decollement beneath the Lorestan Arc is weaker than any such feature beneath the Dezful Embayment, providing an explanation for the plan-view sinuosity of the range-front of the Zagros Mountains.

Key words: Satellite geodesy; Earthquake source observations; Continental neotectonics; Rheology: crust and lithosphere; Asia.

1 INTRODUCTION

On 2014 August 18 an M_w 6.2 thrust-faulting earthquake occurred at Murmuri (sometimes spelt Mormori), near Dehloran in the Zagros Mountains of SW Iran (Fig. 1). This event was followed by five aftershocks with magnitudes ≥5.4, the largest of which was M_w6.0, 16 hr after the mainshock. This sequence of earthquakes provides an opportunity to examine the seismic behaviour of the northwestern Zagros, at the boundary between the Lorestan Arc and the Dezful Embayment (Fig. 1) using a range of seismological and geodetic methods. By studying this earthquake, we can gain insights into a range of open questions regarding the deformation of the Zagros Mountains, and fold-thrust belts in general.

Recent debate has focused on the depth extent of slip in thrust-faulting earthquakes elsewhere in the Zagros Mountains. Nissen *et al.* (2011) suggested that seismic slip is mostly concentrated in the lower part of the 10–15 km thick sedimentary sequence, known as the 'Competent Group', composed of a sequence more than 5 km thick dominated by Mesozoic and Paleozoic platform carbonates. This group is underlain by the Precambrian-Cambrian Hormoz salt in the Fars arc of the southeastern Zagros (Fig. 1), where it reaches the surface in diapirs, but the distribution of salt at depth in the Dezful Embayment and Lorestan Arc is unknown. A small proportion of the earthquakes in the Zagros are thought to rupture the basement, and on rare occasions large events (e.g. the M_w6.7 1972 Ghir and 1977 Khurgu earthquakes in the SE Zagros) rupture both the sedimentary section and basement, and occur in the isolated places where lower Paleozoic rocks are exposed at the surface. However, plentiful aftershocks at basement depths have been recorded following shallower events (e.g. Nissen *et al.* 2011, and references therein). This observation led Barnhart & Lohman (2013) to propose a new view of the depth distribution of the faulting, based upon the analysis of InSAR interferograms of three M_w 5.9–6.0 earthquakes in the SE Zagros. They proposed that seismogenic faulting occurs in the basement, coincident with the majority of the aftershocks, and that the shallower slip inferred from previous models of interferograms was due to aseismic sliding in the post-seismic period. Nissen *et al.* (2014) disputed this view based upon the range of earthquake depths compatible with seismic waveforms. However, it is clear that the depth distribution of faulting within the Zagros

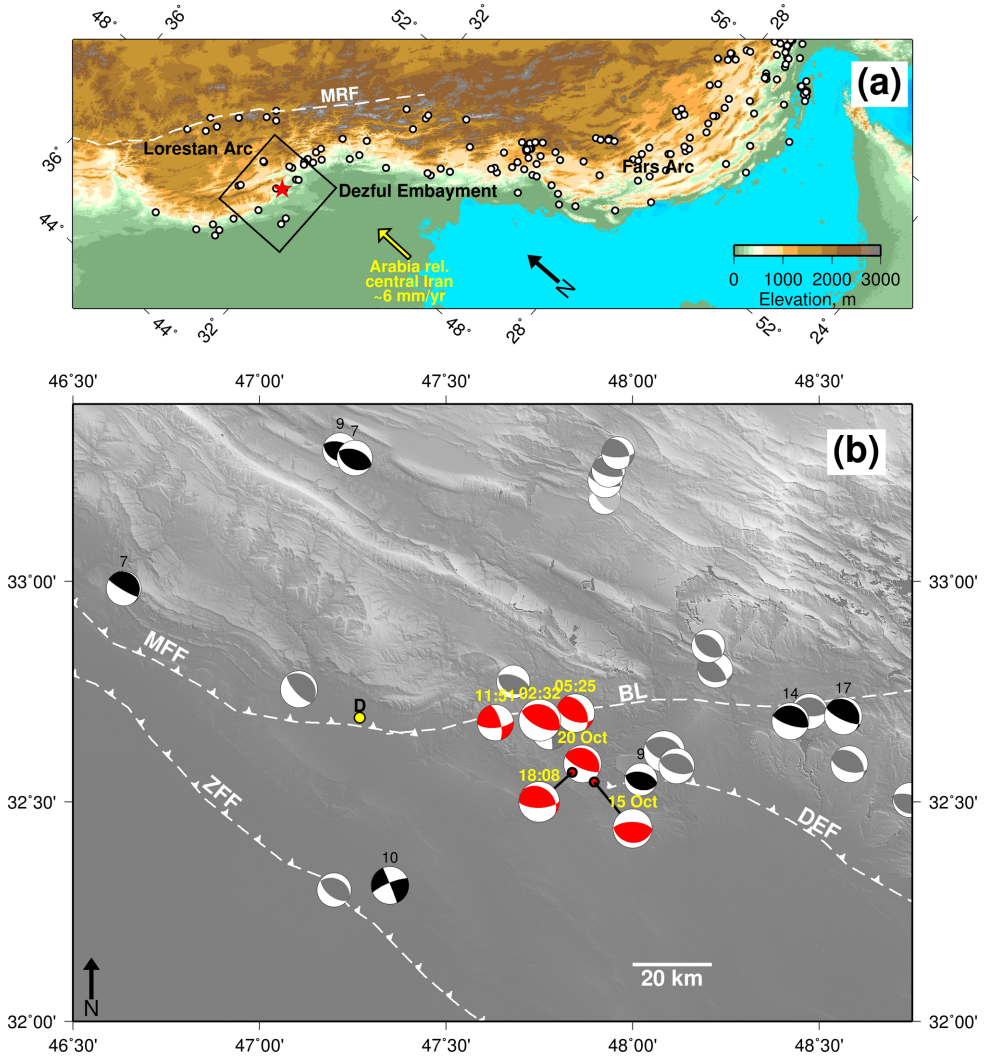

Figure 1. (a) Earthquakes and topography of the Zagros Mountains. White circles show events of magnitude 5.0 and larger from the catalogue of Nissen *et al.* (2011). The red star shows the Murmuri mainshock. The white dashed line marked 'MRF' shows the Main Recent Fault. (b) Earthquakes in the area of the black box on (a), taken from the compilation of Nissen *et al.* (2011) and this study. Black mechanisms were obtained by previous body-waveform modelling studies and are labelled with the depth in kilometres. Dark grey are CMT solutions. Pale grey are from first-motion polarities of *P* waves. The red events are mechanisms calculated by this study for the Murmuri mainshock (2014 August 18) and aftershocks, labelled with the time for events on 18 August, and the date for subsequent events. White dashed lines mark major changes in the stratigraphic level (of 2–6 km, lower to the southwest) and are named the Balarud Line (BL), the Mountain Front Fault (MFF), the Dezful Embayment Fault (DEF), and the Zagros Foredeep Fault (ZFF) (Berberian 1995). The yellow circle marked 'D' shows the location of Dehloran.

Mountains is a source of debate, with wider implications for the distribution of mechanical properties and deformation within this and similar fold-thrust belts. We therefore aim to provide additional insights into this debate by examining an earthquake sequence from a part of the Zagros Mountains which has not seen any other large earthquakes since the development of satellite geodetic methods.

A further open question regarding the tectonics of the Zagros mountains concerns the development of the arcs and embayments that result in a sinuous outline to the range-front in plan view (Fig. 1). It is well known that in the central and NW Zagros the overall oblique convergence between Arabia and Central Iran is partitioned into thrust faulting in the Zagros Mountains and parallel strike-slip faulting along the Main Recent Fault on the NE edge of the range, at the junction with the central Iranian plateau (e.g. Talebian & Jackson (2004); 'MRF' on Fig. 1a). However, to understand the development of the arcs and embayments along the range-front requires a more detailed examination of the direction of motion in thrust earthquakes within the Zagros Mountains. Previous seismological results from earthquakes in the region (Fig. 1b) show low-angle thrusts at mid-crustal depths on the NE margin of the Dezful Embayment (i.e. with centroid depths of 14–17 km) that may represent thrusting on the boundary between the basement and thick sedimentary section. Shallower events with higher-angle nodal planes within the Lorestan Arc may represent thrusting within the sedimentary section, but the tectonic significance of a low-angle thrust on the Lorestan range-front remains ambiguous. All other previous earthquakes in the region do not have sufficiently clear waveforms in teleseismic data to perform detailed body-waveform modelling. Therefore, as the largest instrumentally recorded earthquake on the boundary between the Lorestan Arc and Dezful Embayment (Fig. 1), the Murmuri event presents an important opportunity to examine the tectonics of this region, and address what combination of tectonic forces and material properties can give rise to the overall shape and deformation pattern of the mountain range.

In this paper we address these questions by using seismology and InSAR to investigate the slip that occurred in the 2014 Murmuri earthquake and aftershocks. The mainshock has been previously studied using InSAR by Motagh *et al.* (2015), and in this paper we build upon their work by incorporating additional techniques and datasets to analyse the earthquake sequence. We initially describe results from modelling *P* and *SH* seismic waveforms to obtain the focal parameters of the larger events. We then present seismological relative relocations of the earthquakes in this cluster, to provide information on the spatial distribution of the mainshock and aftershocks. Next, we model InSAR interferograms of the time spanning the earthquakes, and obtain models for the geometry of the faulting that are consistent with both the seismological and geodetic results. Finally, we discuss the implications of our results for the mechanical properties and active deformation of the Zagros Mountains.

2 BODY-WAVEFORM MODELLING

We have jointly inverted *P* and *SH* waveforms to obtain the focal parameters of the six events in the Murmuri earthquake sequence with a sufficiently large signal-to-noise ratio in teleseismic data. We low-pass filter the seismograms in order to reproduce the response of a long-period (15–100 s) WWSSN instrument. We then invert for the focal parameters using Greens functions calculated for a point source, using the MT5 program of Zwick *et al.* (1994) (a version of the algorithm of McCaffrey & Abers (1988) and McCaffrey *et al.* (1991)). This procedure is commonly used, and thorough descriptions can be found in Nabelek (1984) and Taymaz *et al.* (1991). We use a velocity model for these seismic inversions, and for the geodetic inversions described below, which was obtained by a microseismicity study in the Masjed–Soleyman region of the Zagros Mountains, 50–100 km to the SE of the Murmuri earthquake sequence (Nissen *et al.* 2011). This model has *P*-wave velocities of 5.0 km s^{-1} in the top 10 km, 5.95 km s^{-1} at depths of 10–14 km, and then 6.15 km s^{-1} for the remainder of the crust. The *S* velocity was calculated from the *P* using a V_p/V_s ratio of 1.73, and the density was taken to be 2800 kg m^{-3}.

Our preferred solution for the mainshock is shown in Fig. 2. Almost pure thrusting occurred on either a plane dipping NE at 26°, or one dipping SW at 64°. By holding each of the focal parameters fixed at values away from the best fit, and re-inverting for all other parameters, we have estimated the possible errors in the strike to be ±15°, the dip to be ±10°, and the rake to be ±20°. The results of using the same procedure to estimate the centroid depth (the slip-weighted average depth of slip) are shown on Fig. 3, and result in a centroid depth estimate of 2–6 km.

We applied the same method to the five aftershocks with a sufficiently large signal-to-noise ratio, and our solutions for these events are shown in Appendix A. We note that although we describe these events as aftershocks of the Murmuri mainshock, some occurred a significant distance from the mainshock, on distinct geological structures (described in detail below). These events could also be viewed as a second, triggered, mainshock and aftershock sequence. All except one event had thrust-faulting mechanisms, as shown on Figs 1 and 4. The exception is the M_w 5.4 event at 11:51 on 18 August, which was an oblique combination of thrust and strike-slip motion. The estimated focal parameters are listed in Table 1, and the centroid depths are shown on Fig. 3. The focal parameters for these aftershocks are resolved to a similar level of accuracy as the mainshock, except for the more poorly constrained event at 11:51 on 18 August for which the estimated potential errors are roughly twice as large. We will discuss these seismological results in more detail later in this paper, in the context of our estimated hypocentral locations and the InSAR results.

3 EARTHQUAKE RELATIVE RELOCATIONS

We have relocated the teleseismically recorded aftershocks, and the mainshock hypocentre, relative to each other using a multiple event relocation method that has been specialized for studies of calibrated (i.e. bias-free) locations. We used a method based on the Hypocentroidal Decomposition (HD) method (Jordan & Sverdrup 1981) to relatively relocate the events (see Biggs *et al.* 2006; Bondar *et al.* 2008; Nissen *et al.* 2010; Copley *et al.* 2012 for recent applications of this technique). We used teleseismic *P* and *S* phase arrival times reported by the International Seismological Centre (ISC), fixed all hypocentre depths, and solved for the hypocentre latitude and longitude. The HD analysis provides strong constraints on the relative hypocentral locations of all events in the cluster (formal uncertainties are 0.6–1.7 km at the 90 per cent confidence level). The locations of the aftershocks relative to the mainshock hypocentre are shown on Fig. 4, along with the focal mechanisms we obtained by the body-waveform modelling. The initial two large aftershocks occurred within ∼10 km of the mainshock hypocentre, to the east and west. The hypocentres of the other three events large enough to obtain waveform-modelled mechanisms, including the largest aftershock, were clustered together ∼15 km SSE of the mainshock hypocentre. The spatial distribution of the events will be utilized below, and is key to understanding the relationship between the ground motions observed with InSAR and the locations of the mainshock and aftershock fault planes.

If near-source data are available with good azimuthal coverage, or if the locations of one or more events in the cluster of relatively relocated hypocentres are known by independent means, the cluster can then be calibrated to provide absolute hypocentre positions. Given an azimuthal gap in near-source arrival time data of nearly 180° at southern azimuths, we instead calibrate the cluster using InSAR-derived locations of two moderate earthquakes: the 2014 October 15 aftershock (described in Section 7) and an earlier 2008 August 27 strike-slip earthquake that lies ∼40 km SW of the Murmuri sequence, which was observed with InSAR and modelled by Nippress *et al.* (2014). In each instance we fix the hypocentre to the centre of the InSAR model fault plane; for the 2014 earthquake we use the N-dipping plane, though results using the conjugate S-dipping plane were not significantly different. Uncertainties in the positions of the hypocentres on the two model fault planes is an additional source of error in the calibrated locations, and is likely to be on the order of 5 km (i.e. the radius of the rupture patch in the calibration events). In the following sections the main contribution from this relocation work is based on the relative locations of the mainshock and aftershock hypocentres. We therefore interpret the better-constrained relative locations, rather than the InSAR-calibrated absolute locations, but return to the estimates of the absolute locations in the discussion section.

4 InSAR RESULTS

Interferograms for the time period covering the earthquakes were produced by Motagh *et al.* (2015) using data from the Radarsat-2 satellite. Two interferograms were made, covering the eastern and western parts of the epicentral area, with a small overlap. Both

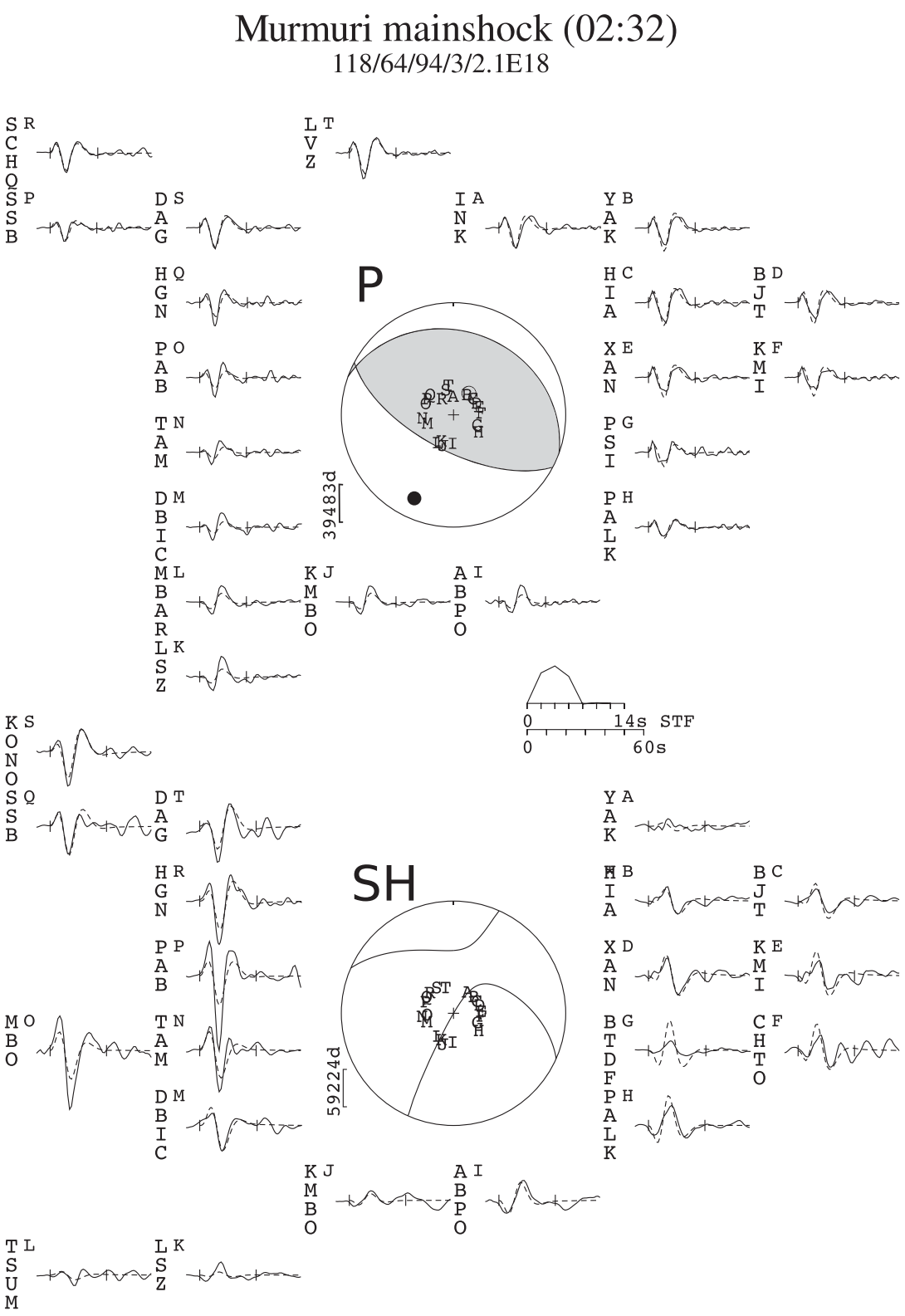

Figure 2. Mechanism of the Murmuri mainshock, from the inversion of *P* and *SH* body waves. The event header shows the strike, dip, rake, centroid depth and scalar seismic moment (in Nm) of the minimum misfit solution. The top focal sphere shows the lower hemisphere stereographic projection of the *P* waveform nodal planes, and the positions of the seismic stations used in the modelling routine. The lower focal sphere shows the *SH* nodal planes. Capital letters next to the station codes correspond to the position on the focal sphere. These are ordered clockwise by azimuth, starting at north. The solid lines are the observed waveforms, and the dashed lines are the synthetics. The inversion window is marked by vertical lines on each waveform. The source time function (STF) is shown, along with the timescale for the waveforms. The amplitude scales for the waveforms are shown below each focal sphere. The P and T axes within the P waveform focal sphere are shown by a solid and an open circle, respectively.

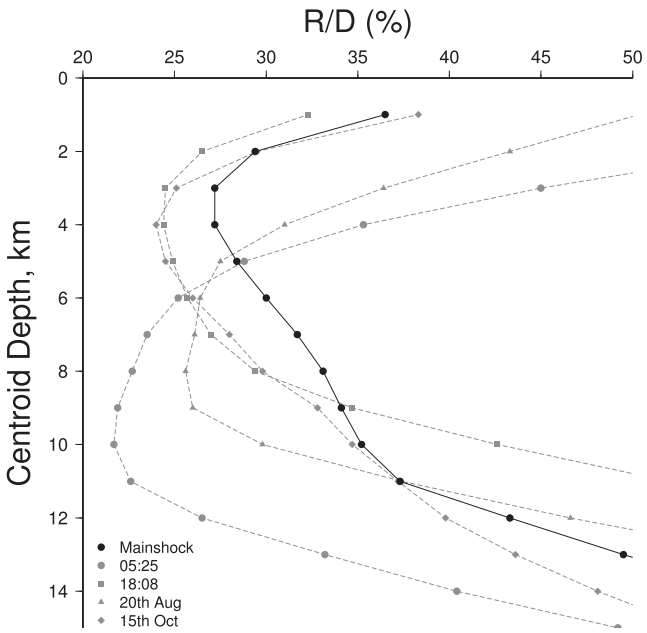

Figure 3. Plot of misfit (expressed as a percentage of the variance in the data) as a function of centroid depth for the Murmuri mainshock and the larger aftershocks.

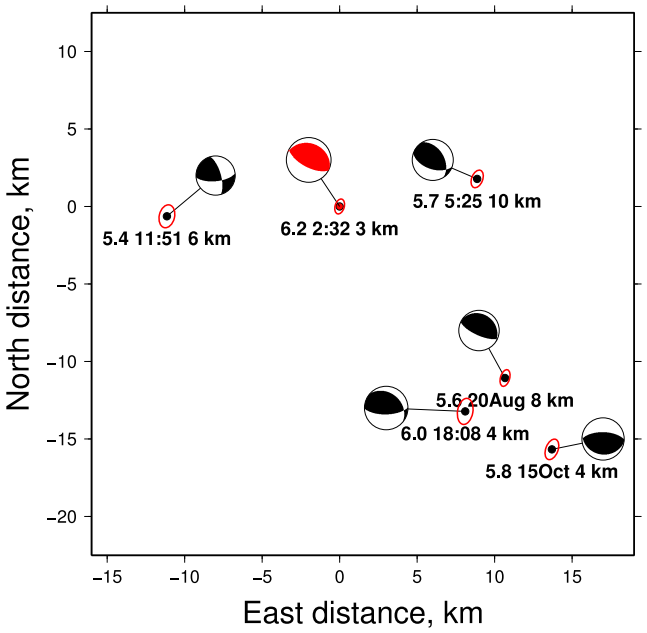

Figure 4. Hypocentral locations of the largest aftershocks in the Murmuri earthquake sequence, relocated relative to the mainshock hypocentre (shown in red) using the methods described in the text. The red ellipses give the formal 90 per cent confidence estimates for the relative locations, which have semi-major axes of length $\leq$1.7 km. The focal mechanisms were obtained from our body-waveform modelling and are offset from the locations for clarity. The mechanisms are labelled with the magnitude, the origin time (as hour:minute for those on 18 August, or the date for subsequent events) and the centroid depth calculated from our waveform inversions.

interferograms were made using ascending-track data, so the line-of-sight between the satellite and the ground is similar for the two interferograms (the 7° difference being due to the across-track variation in look angle). We use these same interferograms in our study, which cover 2012 December 2 to 2014 September 11, and 2013 May 2 to 2014 August 25. The interferograms therefore cover all of the events that were large enough for us to obtain seismological solutions (Table 1) with the exception of the aftershock on October 15.

There are topographically correlated signals present in the interferograms, with the original radar signals mirroring the outline of anticlines and river valleys in each of the interferograms. Local correlation coefficients between the signal and topography were in places as high as 0.9, and the magnitude of these phase gradients with elevation was up to 7 cm km^{-1}. Given the peak line-of-sight displacement for the earthquakes was 15–17 cm, and the topography in the deformation area varies from 100–1000 m (and up to 2500 m in the far-field), it was necessary to remove the topographically correlated noise. We therefore applied a simple linear empirical correction to the interferograms to remove the effect of atmospheric noise (e.g. Elliott *et al.* 2008), before modelling the deformation signals. To avoid aliasing between the earthquake deformation field and the topographic correction, we calculated the elevation–phase gradients in regions 20–40 km away from the deformation area. To remove long-wavelength orbital errors in the interferograms, each was flattened by removing a quadratic polynomial for the entire scene, after the atmospheric correction had been made to the data. This process is equivalent to the procedure used by Motagh *et al.* (2015), who removed a bilinear ramp and an elevation-dependent term from the interferograms, and demonstrated the robust presence of earthquake-related displacements following this procedure.

The atmospherically corrected interferograms are shown in Fig. 5, and display a complex pattern with two lobes of displacement extending ∼E and ∼SE from the maximum-displacement patch (of ∼15 cm). The magnitude of non-tectonic signals in the interferograms can be estimated by examining areas distant from the ground motion patch associated with the earthquake sequence. The standard deviation of the data in these regions is 1.1 cm.

5 FAULT GEOMETRY MODELLING

5.1 Single or multiple faults?

The smooth signals in the interferograms, with no major discontinuities, show that the causative fault slip was buried at depth. The initial question to be addressed using the geodetic data is whether the slip that generated the surface motions occurred on one plane, or multiple faults.

Following Motagh *et al.* (2015), we initially find the single uniform-slip fault plane that best fits the surface displacements. This initial estimate for the fault geometry (strike of 298° and dip of 28°) is within 6° of strike and 1° of dip of that of Motagh *et al.* (2015), and is consistent with the NE-dipping plane in the seismological solutions. We then invert for the distribution of slip on this plane that provides the closest match to the InSAR results. We discretize the fault plane into 2 km × 2 km square patches, and the inversions are performed using a simulated annealing algorithm to find the model that best fits the geodetic data (for a more complete description of the method used, see Ji *et al.* (2002) and Konca *et al.* (2008, 2010)). For computational efficiency, the InSAR data was down-sampled using a Quadtree algorithm (see Jonsson *et al.* (2002) and Wright *et al.* (2004) for detailed descriptions of this method). We find a similar distribution of slip to that obtained by Motagh *et al.* (2015), as shown in Fig. 6. However, we find that such a model is unable to fit the short-wavelength component of the surface deformation field, especially the double peak in the surface

Table 1. Focal mechanisms obtained in this study from body-waveform modelling.

Date and time	Strike	Dip	Rake	M_0 (Nm)	Centroid depth (km)
18-08-2014 02:32	289	26	82	2.1×10^{18}	3^{+3}_{-1}
18-08-2014 05:25	329	44	121	2.4×10^{17}	10^{+2}_{-4}
18-08-2014 11:51	344	68	154	1.3×10^{17}	<10*
18-08-2014 18:08	310	28	130	7.2×10^{17}	4^{+3}_{-2}
20-08-2014 10:14	308	20	103	1.5×10^{17}	8^{+2}_{-3}
15-10-2014 13:35	271	63	87	6.1×10^{17}	4^{+3}_{-2}

*Depth poorly constrained. Less than 10 km, with a nominal best-fit at 6 km.

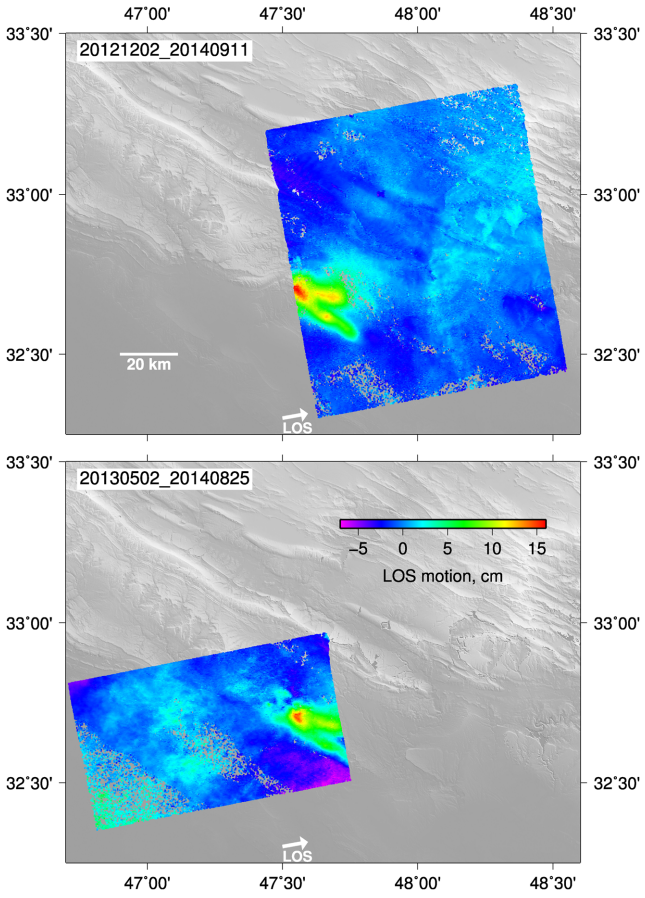

Figure 5. Atmospherically corrected unwrapped interferograms, equivalent to fig. 2 of Motagh *et al.* (2015). Each interferogram is labelled with the dates of the two SAR acquisitions in the format YYYYMMDD, and the background shading is the topography. Motion is in the satellite line-of-sight, inclined at ∼45° to the vertical and in the direction marked 'LOS'. Positive values correspond to motion towards the satellite.

motions in the region of the eastern displacement lobes crossed by profile Y–Y′ in Fig. 6. This feature of the inversion results was also seen by Motagh *et al.* (2015) (their fig. 2c and f). Spatially organized misfits are present that follow the shape of the deformation patch. This result is not due to any smoothing constraints imposed on the slip distribution (we purposefully investigated rough solutions, to ensure this is not the case), but to the depth of fault slip. The model fault plane is at a depth of 5–10 km beneath the northernmost lobe of slip, so motion on this plane is unable to match the short-wavelength features that dominate the surface displacement field. This effect occurs because the displacements are smoothed by the presence of the overlying elastic crust, resulting in considerably wider surface deformation features than are observed in the InSAR results.

The inability of a single-fault model to match the surface deformation pattern implies that slip on more than one plane produced the surface deformation observed by InSAR. Such a situation is also implied by our seismological results: the M_w6.0 aftershock had a centroid depth of 4^{+3}_{-2} km, and an event of this magnitude and depth would be expected to produce significant surface motions visible to InSAR. In the following section we therefore investigate whether the displacement field can be adequately fit with a multiple-fault model, with the fault planes corresponding to the mainshock and one or more of the aftershocks (the largest of which was separated from the mainshock by ∼15 km; Fig. 4).

5.2 Fault dip directions

In light of the inversions for slip on a single fault described above, the two distinct lobes extending to the east and southeast of the main displacement patch (Fig. 5) suggest that the ground displacements were caused by slip on at least two faults. The clear displacement maximum in the western part of the ground motion patch implies significant along-strike variability in slip on at least one of these two planes, or the presence of a third fault plane. We therefore initially model the displacements using three uniform-slip rectangular fault planes. This configuration could represent the presence of two fault planes, and along-strike slip variation on one of them (which represents the simplest arrangement of faulting that can fit the main features of the data), or the presence of three faults. We will first describe the results of these inversions using uniform-slip rectangular planes, and then perform inversions for the distribution of fault slip once our initial inversions have provided constraints on the geometry of the faulting.

We have performed inversions in which the uniform-slip rectangular faults all dip north, all dip south, or have a combination of dip directions. We use a simulated annealing inversion algorithm in which the parameters of the fault planes are progressively updated through the inversion procedure, but have a progressively decreasing possibility of moving to a worse solution. Such a method is designed to avoid the inversion routine being confined to a local minimum. We invert for the strike, dip, rake, length, location, depth extent, and slip on the three planes, and also for an offset relative to zero and a linear ramp in each of the two interferograms. We find that the misfit between the data and the models is similar for inversions in which the faults all dip north, all dip south, or have a combination of dip directions. The RMS misfits are in the range 0.92–0.93 cm. The standard deviation of the signals in the interferogram in the areas away from the tectonic signal is 1.1 cm, which gives the size of the non-tectonic noise in the data. (For comparison, the uniform-slip single-fault inversions described above resulted in an RMS misfit of 1.5 cm.) The similarity between the misfits of the

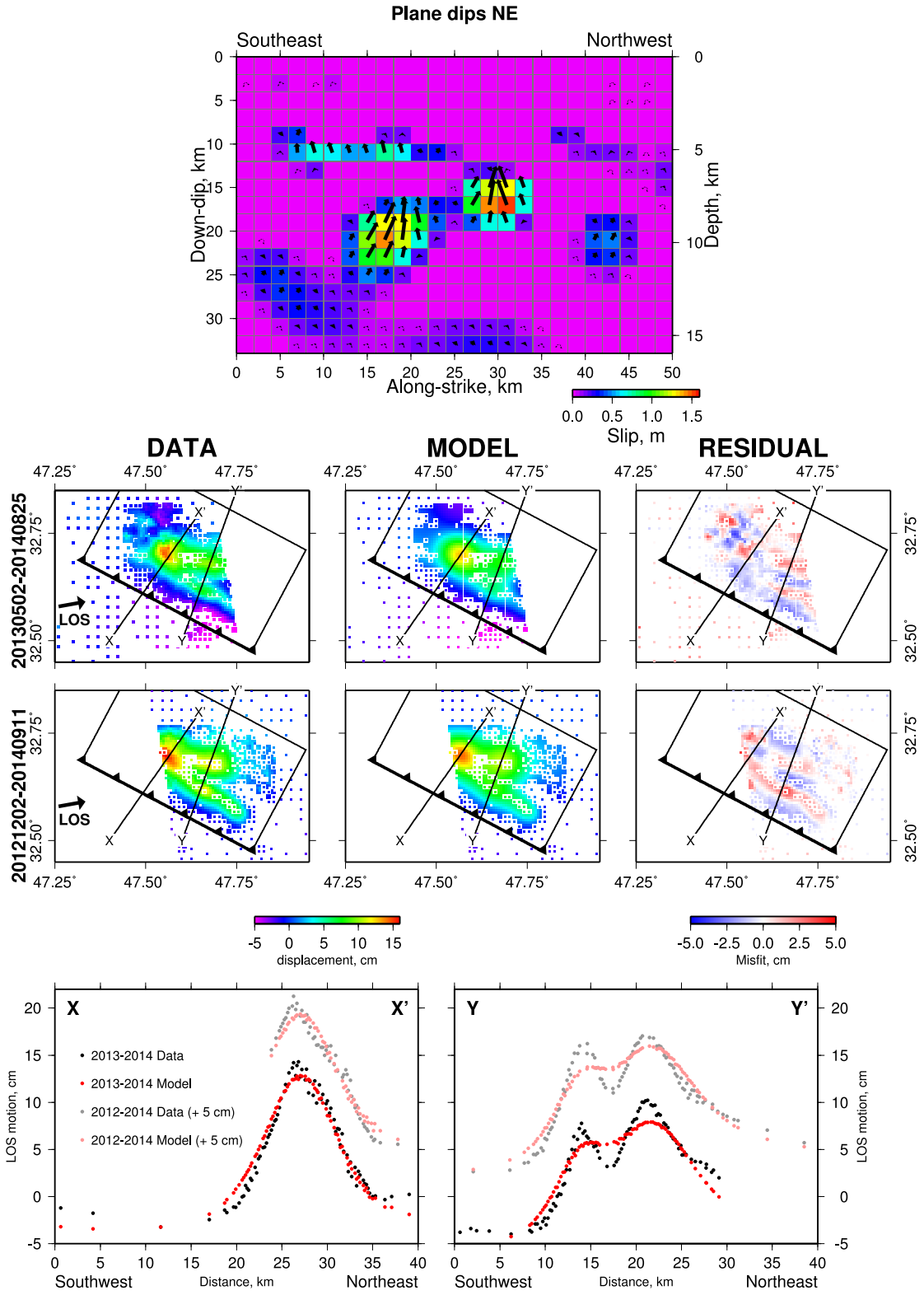

Figure 6. Results of inversions for the distribution of slip on the Murmuri fault plane, assuming slip occurred on a single plane that dips to the north. The upper panel shows the estimated slip distribution, viewed looking downwards from an angle normal to the plane. The depth measured perpendicular to the Earth's surface is shown, along with the distance downdip on the fault plane. The colour represents the amount of slip, and the arrows show the direction of motion of the hangingwall relative to the footwall. The centre panels show the InSAR data, model and residuals for the two interferograms. The black rectangle shows the surface projection of the outline of the fault plane with the thick line with teeth showing the updip edge of the fault plane. The lower panels show profiles through the data and model along lines X–X′ and Y–Y′. Note the significant misfit between the models and the data on profile Y–Y′, where the model is unable to match the double peak seen in the InSAR data. The small amounts of slip in the deeper parts of the fault plane (i.e. >25 km downdip) are likely to represent an inversion artefact, as the available InSAR data are not very sensitive to the amount of slip on this part of the fault plane.

models and this measure of the noise in the interferograms implies that the models are fitting the tectonic signal to the level required by the quality of the data, and that the differences between the misfits of the models are not significant.

We have resolved the ambiguity in fault dip direction by using the information provided by the seismological results. We have re-run the inversions described above, but limited the possible ranges of the strike, dip, and rake of the fault planes to be those consistent with the results of the seismological body-waveform modelling. In order to do this we need to ascribe each fault plane to an earthquake. The body-waveform inversions show that the two largest events were also the shallowest (i.e. the mainshock and the M_w6.0 aftershock; Fig. 3), and will dominate the surface displacement field. The seismological relative relocations (Fig. 4) show the relative positions of the mainshock and largest aftershock, specifically that the mainshock hypocentre was ∼15 km to the NNW of this aftershock. We therefore apply the mainshock parameters to a fault plane with a starting location in the inversions of beneath the northern displacement lobe seen in the InSAR data (Fig. 5). The parameters of the M_w6.0 aftershock are applied to a southern fault plane, positioned beneath the southern displacement lobe. In our initial inversions, the third fault plane was found to correspond to a small area (∼3 × 3 km) close to northernmost fault, implying that the slip required to produce the displacement peak was probably a high-slip patch on the northernmost plane, which would require two planes to model in these inversions using uniform-slip on rectangular planes. (The moment release on this third plane is too large to represent any of the smaller, unmodelled, aftershocks.) Such a geometry is consistent with the northernmost plane representing the mainshock fault plane, and also consistent with inversions for the distribution of slip on the fault planes described below. We therefore also constrain the third fault plane to have our seismologically derived mainshock fault parameters.

We find that configurations with all fault planes dipping south are unable to produce a good match to the InSAR displacements, due to the strike of the southern displacement lobe being incompatible with the range of possible strikes of the south-dipping plane in the seismological inversions for the largest aftershock. Fig. 7 shows the best-fitting model in which all fault planes dip north. The gentle displacement gradient at the northern end of profile Y–Y′ shown on Fig. 7h (i.e. at distances along the profile of greater than 25 km), is well fit by the displacements due to faults dipping north. This feature is higher in amplitude than the non-tectonic signals in the interferograms, and appears on both, independent, interferograms, so is likely to represent true tectonic ground motion. Models in which the northern displacement lobe is fit with a south-dipping fault, with strike, dip, and rake consistent with the seismological results, produce displacement gradients in this area that are too steep to fit the data. An example of such a model is shown in Appendix B. We therefore conclude that the surface motions were produced by north-dipping faults. The misfits for models in which the mainshock fault-plane dips south are 10 per cent greater than those in which the plane dips north. The third, small, fault-plane is positioned in almost the same place as the main northern fault plane in these inversions, implying that it represents a high-slip patch on the same plane. The relative positions of the northern and southern fault planes in these inversions are consistent with the 15 km NNW/SSE offset between the hypocentres of the mainshock and largest aftershock in our seismological relative relocations, further supporting the use of multiple planes to model the surface deformation. The parameters of the fault planes are listed in Table 2.

The depth extent of slip in the inversions of the InSAR data was not imposed to be consistent with the seismological results. However, the centroid depths of the seismic and geodetic models are in agreement within error (Tables 1 and 2). The moment release is larger in the geodetic results than the seismological results (by ∼40 per cent, including the seismological moments of only those earthquakes that occurred during the geodetic observation period). This feature is often seen for events in the Zagros Mountains and Makran (e.g. Lohman & Simons 2005; Nissen *et al.* 2010; Roustaei *et al.* 2010; Penney *et al.* 2015), and is usually interpreted to represent post-seismic afterslip contributing towards the geodetically measured moment, or systematic errors in the velocity models used. In addition, because the available InSAR data has only one look-angle for the Murmuri events, it should also be noted that the rake in the geodetic inversions is relatively poorly constrained (and reliant on the imposed seismological limits), so the moment in the InSAR inversions will be subject to a trade-off between the rake and the amount of fault slip.

The intensity VII shaking zone from the earthquakes was elongated in a N–S direction, consistent with our fault geometry consisting of multiple planes positioned across-strike from each other in a ∼N–S direction. The majority of injuries and damage from the 18:08 aftershock were in the southern part of the damaged area, consistent with the positioning of this event to the south of the mainshock in our seismological and geodetic results.

6 DISTRIBUTION OF SLIP

Using the fault geometry obtained in the previous section, we have inverted the InSAR data for the distribution of slip on the fault planes. In order to combat the ambiguity in rake that can occur when observations from only one InSAR look-angle are available, we impose the seismologically derived limits on the range of rakes that can be present in our inversions. We invert for the distribution of slip and rake that best fit the InSAR displacements using the simulated-annealing-based method described in detail by Ji *et al.* (2002) and Konca *et al.* (2008, 2010). We do not include seismic waveforms in this inversion (as is possible using this routine) because the small spatial size of the ruptured patch means that limited additional information regarding the spatial location of rupture can be obtained by using teleseismic waveforms, and no locally recorded seismograms are available. We use fault planes that are extended laterally and vertically from the uniform-slip inversion results, in order to avoid artificially constraining the extent of slip. The inversion is regularized by imposing a Laplacian smoothness constraint, which we have varied between successive inversions. Our preferred model is on the apex of the curve relating model roughness and misfit to the data (shown in Appendix B), in common with a range of other studies that use a variety of methods to choose the optimum point on this curve (e.g. Freymueller *et al.* 1994; Johanson & Burgmann 2010). We do not interpret any features that are significantly different between the models on different parts of this apex (such as the rougher and smoother solutions shown in Appendix B). Our preferred model is shown in Fig. 8. The depth extent of slip is consistent with the seismological and initial geodetic modelling described above. Slip on both planes is elongated in the horizontal direction—a feature we will discuss in more detail below. The source models predict the earthquake slip to have remained buried at depth, consistent with the lack of primary surface ruptures observed during post-earthquake fieldwork in the region by one of us (BO). The misfit to the data is 0.9 cm, similar to the level of

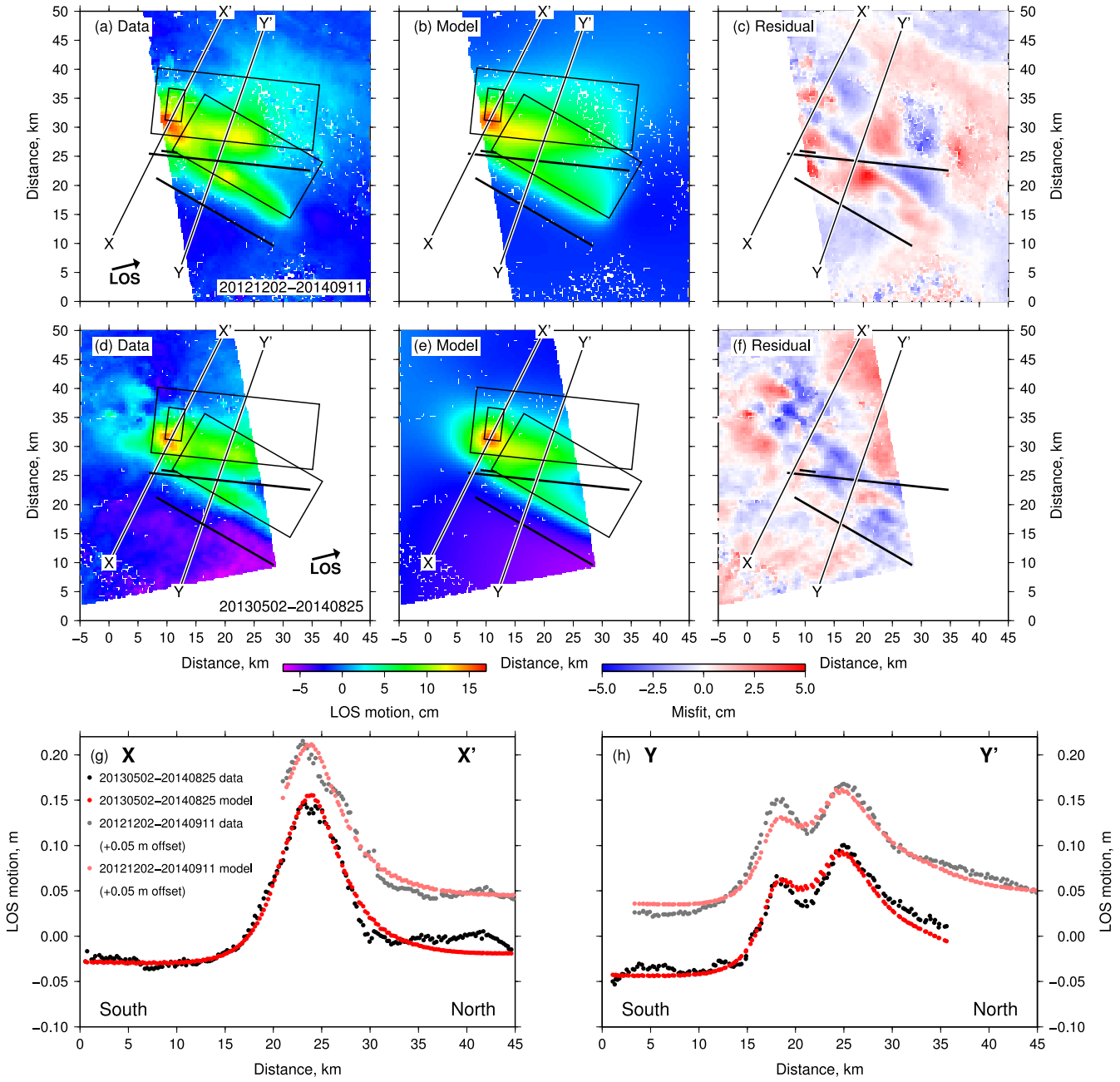

Figure 7. Data (a,d), model predictions (b,e) and residuals (c,f) for a model of the InSAR displacements constructed using uniform-slip rectangular planes. Black rectangles show the locations of the fault planes. The associated thick black lines show the surface projections of the fault planes, projected updip to the surface. (g,h) Profiles through the interferograms and the models along the lines X–X′ and Y–Y′. The points relating to the 20121202–20140911 interferogram have been offset by 0.05 m for clarity.

Table 2. Geodetic inversion results for uniform-slip models.

Plane	Strike	Dip	Rake	M_0 (Nm)	Centroid depth (km)	Top depth (km)	Bottom depth (km)	Length (km)	Slip (m)
Large northern	276	34	60	2.3×10^{18}	6.2	2.4	10.0	28	0.19
Small northern	277	26	100	3.0×10^{17}	4.0	2.6	5.3	3	0.57
Southern	300	21	101	2.1×10^{18}	4.3	2.1	6.4	23	0.25

non-tectonic signal in the interferogram in areas distant from the earthquake.

The horizontal length of the slip patch on the northernmost (mainshock) fault plane is ~20 km. This estimate is consistent with the 8 s length of the source time function in the seismological inversions, if this duration represents the time required for the rupture to propagate along the length of the fault at typical rupture velocities (e.g. 2–3 km s^{-1}). The displacement-length ratios for the slip patches on

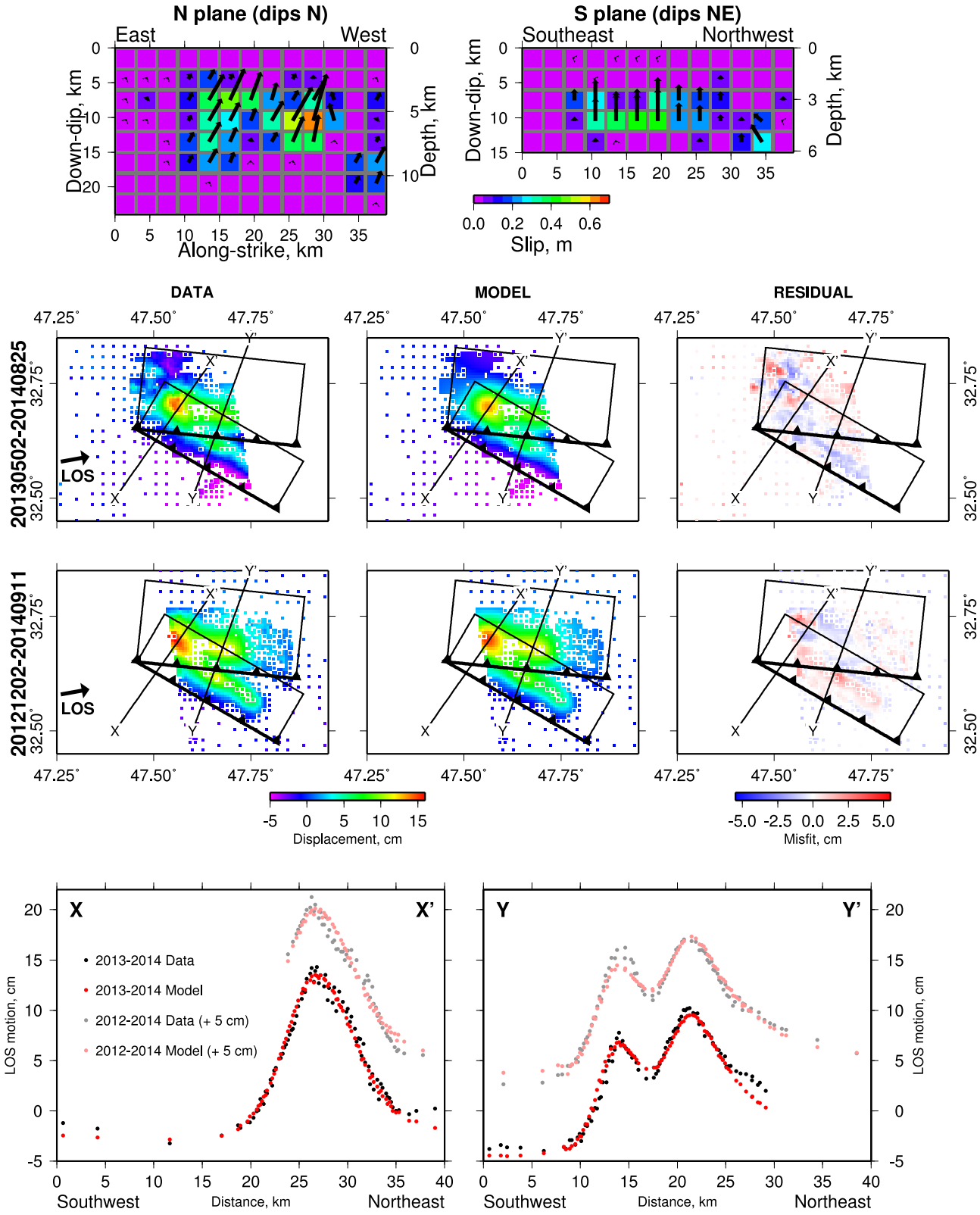

Figure 8. Results of inversions for the distribution of slip on the fault planes. The upper panels show the estimated slip distributions on the northern and southern planes, viewed looking downwards from normal to the planes. The depth measured perpendicular to the Earth's surface is shown, along with the distance downdip on the fault plane. The colour represents the amount of slip, and the arrows show the direction of motion of the hangingwall relative to the footwall. The centre panels show the data, model and residuals for the two interferograms. The black rectangles show the surface projections of the outlines of the two fault planes, with the thick lines with teeth showing the updip edges of the fault planes. The lower panels show profiles through the data and model along lines X–X′ and Y–Y′. The small amounts of slip in the deeper parts of the western edges of both fault planes are likely to represent inversion artefacts, as the available InSAR data are not very sensitive to the amount of slip on this part of the fault plane.

both planes are 2–4 × 10^{-5}, which is within, but towards the lower end of, the range often observed for earthquakes (e.g. Scholz 1982; Scholz *et al.* 1986).

7 15 OCTOBER AFTERSHOCK

A further Radarsat-2 interferogram covers the time period 2014 September 11 to 2014 October 29, and includes the location of the 15 October aftershock (Table 1). A small but visible signal of up to 4 cm is present in the location of the aftershock, with a strike that is consistent with the seismological estimates. Models of this aftershock are shown in Appendix C, and either north- or south-dipping solutions are within error of the seismologically derived focal parameters. The buried nature of the slip, and the asymmetry in the displacements being swamped by the noise in the data, mean that there is no clear way to establish if the fault plane dipped to the north or south.

8 DISCUSSION

Fig. 9 summarizes the deformation that occurred in the Murmuri earthquake sequence. The focal mechanisms of the mainshock and largest aftershock are plotted at their relocated hypocentre positions (Section 3). Both hypocentres are positioned at the SE end of their respective rupture patches (shown as solid and dashed black outlines), implying that rupture propagated to the W/NW in both events. The area of uplift observed by InSAR is shown as a dashed red outline. There is an offset between the location of the NE part of the mainshock rupture patch (solid black outline on Fig. 9) and the axis of the Dal Parri anticline (NW–SE pale blue line). However, the updip projection of the fault lies close to the anticline axis. This relationship is as expected: interseismic strain accumulation and coseismic slip will balance each other in the rocks bounding the fault over an entire earthquake cycle, resulting in an overall raising of the level of the hangingwall but not the construction of short-wavelength (∼5 km) topography and geological structures such as the anticlines. However, these features can be produced by other deformation mechanisms that contribute to the earthquake cycle, such as bedding-plane slip during earthquakes (e.g. Berberian 1979) and post-seismic slip (e.g. Copley & Reynolds 2014). It would therefore be expected that anticlines expressed at the surface would be positioned close to the updip limit of earthquake rupture, in the region that must deform at other times in the earthquakes cycle in order to accommodate the slip at depth. This configuration is observed in the region of the Murmuri earthquake sequence: there is a an elevated but low-relief area above the mainshock slip patch, and the anticline axis is close to the updip limit of seismic slip (Fig. 9). There is a closer correspondence between the aftershock slip-patch (dashed black outline) and the anticline axis, which is likely to be because the majority of the aftershock slip was at the same depth interval as the shallowest mainshock slip (Fig. 8), so the observed geometry is consistent with the surface anticlines being positioned close to the updip limit of earthquake slip.

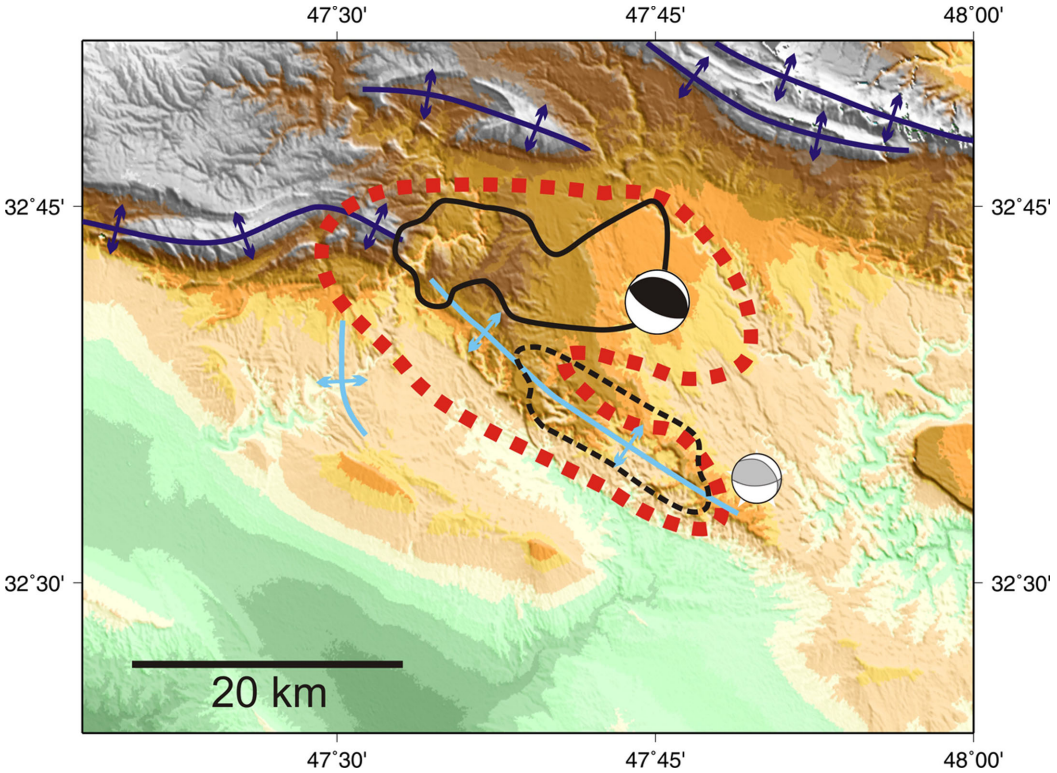

Figure 9. Summary of deformation during the Murmuri earthquake sequence. The red dashed outline shows the area of significant ground uplift observed by InSAR. The solid and dashed black lines show the smoothed outlines of areas of significant slip on the mainshock (north) and aftershock (south) fault planes, respectively. Both planes dip to the north. The black and grey focal mechanisms show the seismologically derived mainshock and largest aftershock focal mechanisms, plotted at their relocated positions (Section 3). Purple lines with double-arrows show anticlines expressed at the surface in the Asmari formation (Oligocene/Miocene) and older rocks, and mostly have limbs dipping at ≥20°. Blue lines with double arrows show anticlines where the surface geology is Miocene/Pliocene and younger (i.e. Agha Jari formation and overlying units) and mostly have limbs dipping ≤20°. Structural information from Geological Survey of Iran (1973).

The Murmuri earthquake sequence shows some similarity to a series of strike-slip earthquakes in 1958 on the Main Recent Fault near Firuzabad. A sequence of M_w5.5 and 5.7 earthquakes on 14 August, and an M_w6.5 event on 16 August, also ruptured multiple fault segments in close succession. The magnitude 5 events were on a fault positioned across-strike from that which ruptured in the 6.5 (Berberian 2014), in a similar manner to the across-strike positioning of the Murmuri mainshock and aftershock fault planes.

8.1 Depth of slip and sedimentary stratigraphy

In both uniform-slip and distributed-slip inversions of the InSAR data, the fault slip is concentrated at depths of ∼2–10 km in the best-fitting models (Figs 7 and 8), and the misfits between the models and the data become prohibitively large if the base of the faulting extends beneath ∼14 km. This result is consistent with the seismological estimates of the mainshock and aftershock centroid depths (Fig. 3), indicating that the geodetic data are imaging the coseismic slip, possibly along with some component of early post-seismic afterslip.

The depth to the basement in the region of the Murmuri earthquake sequence is only poorly known, as with many other areas of the Zagros mountains. Casciello *et al.* (2009) constructed a stratigraphic column based upon field and well data and a survey of the literature. They estimated the top of the basement to be at a depth of ∼13 km. The lack out outcrop of units in the lower part of the sequence, and the scarcity of seismic data, make this estimate imprecise. However, Morris (1977) estimated a similar value of 12 km to the depth of the magnetic basement, presumed to represent the Precambrian crystalline rocks underlying the thick sedimentary section. The nature of the sediment-basement interface is also debated. Indirect evidence relating to the surface gradient of the mountain range has been used to imply the presence of a decoupling horizon (e.g. McQuarrie 2004; Carruba *et al.* 2006). It is not known whether this proposed decoupling horizon represents the same Hormoz Salt that underlies the SE Zagros: unlike that area, there are no salt diapirs reaching the surface in the Lorestan Arc and Dezful Embayment, which has led to the suggestion that any decoupling may result from a thinner salt layer, or an alternative lithology.

From the perspective of relating the slip in the Murmuri earthquakes to the structure of the crust, what seems clear is that the majority, and possibly all, of the seismic slip occurred within the sedimentary sequence. The base of the mainshock fault plane could have reached the basement, but the data do not require this, and the best-fitting models have faults that are shallower than the estimated basement depths. The depth-extent of slip on the southern fault plane, thought to represent the largest aftershock, was 2 to ≤6 km, implying that this event nucleated within, and was entirely contained within, the sedimentary sequence. The inversions of *P* and *SH* waveforms are incompatible with a significant proportion of the seismic slip being at basement depths (Fig. 3).

Previous work has suggested the presence of numerous decoupling horizons within the sedimentary sequence, at depths of ∼3–9 km (e.g. Casciello *et al.* 2009). From our results, it appears that the Murmuri earthquake rupture propagated across these horizons. The upper limit of slip (∼2 km) could have been limited by the evaporites of the Gachsaran formation (∼2–4 km), or this depth agreement could be coincidence, and mark the transition from consolidated seismogenic sediments to relatively incompetent rocks that deform by other mechanisms (e.g. pressure solution creep or aseismic slip).

An unusual feature of the slip distribution in the Murmuri earthquake sequence is that the slip patches are considerably longer along-strike than downdip (Fig. 8). This feature is in contrast to the equidimensional ruptures often observed in earthquakes in a range of tectonic settings (e.g. Wald *et al.* 1996; Ji *et al.* 2003; Avouac *et al.* 2006; Cheloni *et al.* 2010; Copley *et al.* 2012; Elliott *et al.* 2013), including individual high-slip patches in some subduction zone megathrust events (e.g. Chlieh *et al.* 2007; Delouis *et al.* 2010). Horizontally elongated slip patches have been noted for other earthquakes in the Zagros Mountains (Elliott *et al.* in press), and may imply that the vertical extent of the rupture has been constrained by rheological boundaries, possibly related to contrasts in lithology.

A geologically notable feature of the Murmuri earthquakes is that they occurred close to the Balarud Line (the dashed line marked BL on Fig. 1). It has previously been suggested that the Balarud Line represents a region of strike-slip faulting (e.g. Berberian 1995; Hessami *et al.* 2001). However, in agreement with Talebian & Jackson (2004) we find that the earthquakes in this region represent thrust-faulting, so it seems unlikely that the Balarud Line represents a region of active strike-slip faulting. The Balarud Line, along with the Mountain Front Fault (MFF on Fig. 1), Dezful Embayment Fault (DEF) and Zagros Foredeep Fault (ZFF), mark dramatic changes in the stratigraphic level, which is 2–6 km lower on the southwestern sides of the structures (Berberian 1995). These changes in level are thought to represent the locations of major thrust faults in the basement that offset the overlying sedimentary section, and partly controlled sedimentation during the Tertiary. A notable feature of the Murmuri earthquakes in this regard is that we have not observed any seismic slip that is unequivocally at basement depths. Although the earthquakes were close to the mapped locations of the basement faults, they were at shallower depths, so there is still no evidence of significant ($M_w \geq 5$) earthquakes on the proposed basement faults. This observation implies that the basement faults either slip aseismically, or in rare large earthquakes, or that the change in stratigraphic level is accomplished by thickening within the sedimentary sequence rather than by offsets in the underlying basement. Allen & Talebian (2011) suggested that the Balarud Line is at least in part depositional rather than tectonic. The northwestern limit of mainshock slip lies close to the change in stratigraphic level (i.e. the transition from anticlines cored at the surface by Oligocene and older rocks to those exposed in Miocene/Pliocene and younger units; Fig. 9). This geometry could be coincidental, or could suggest that the faults are discontinuous across this boundary and limit the propagation of earthquake ruptures.

8.2 Slip vector azimuth and large-scale tectonics

The Murmuri earthquakes provide an opportunity to investigate the large-scale tectonics of the NW Zagros. The spatial separation of the strike-slip and thrust components of the overall Arabia-central Iran motion onto parallel and spatially separated structures in the Zagros is well known (e.g. Talebian & Jackson 2004), and the thrust mechanisms of the Murmuri earthquakes are consistent with this pattern.

A more subtle question involves asking what controls the arcuate edge of the topography in the Zagros, and whether this geometry has an effect on the deformation. Fig. 10 shows the slip vectors of thrust earthquakes within the NW Zagros, expressed as the motion of the northeast side of the fault relative to the southwest. Only estimates from earthquakes greater than M_w5.0 with well-constrained mechanisms are shown. These solutions are from either body-waveform modelling results, well-constrained CMT solutions (with a percentage double-couple greater than 80 per cent, as defined by Jackson *et al.* (2002)), or first-motion focal mechanisms with sufficient

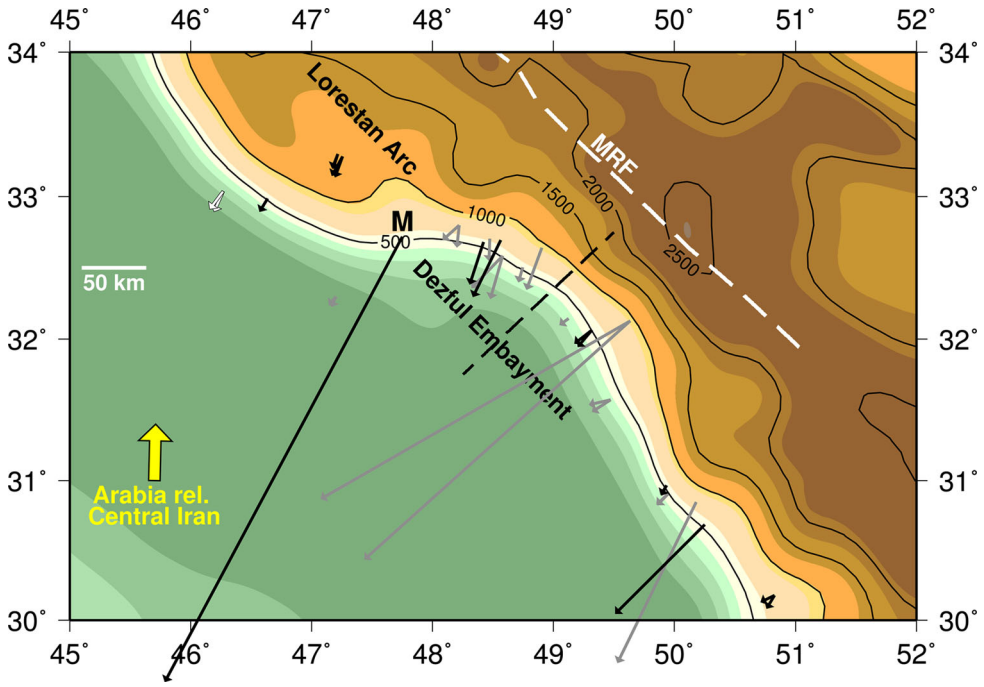

Figure 10. Topography and thrust earthquake slip vectors in the Dezful Embayment and Lorestan Arc. Yellow arrow gives the orientation of the Arabia-Central Iran convergence (e.g. Walpersdorf *et al.* 2006). The dashed white line marked 'MRF' shows the Main Recent Fault, which accommodates the belt-parallel component of the overall motion (e.g. Talebian & Jackson 2004). Topography is filtered with a Gaussian filter of radius 50 km (3-sigma). Arrows are seismologically derived slip vector azimuths (northeast side relative to southwest side) scaled according to seismic moment. The smallest events shown are M_w5.0, and the largest arrow, marked 'M' represents the Murmuri mainshock (M_w6.2). Both possible slip vectors are shown for events where the fault plane is not known. Where thrust events have one very low-angle nodal plane, and one near-vertical plane, it has been assumed that the fault plane has a shallow dip. Black arrows show results from body waveform modelling (from the catalogue of Nissen *et al.* (2011) and this study), grey from well-constrained CMT solutions (with a percentage double-couple greater than 80 per cent, as defined by Jackson *et al.* (2002)), and white arrows show a first-motion result where the polarity observations tightly bracket the nodal plane geometry (Jackson & McKenzie 1984). Slip vectors from aftershocks are not included due to the likelihood of the fault motion direction being affected by stress changes from the associated mainshock in addition to the large-scale tectonic forces. The dashed black line divides earthquakes into groups with different dominant slip vector orientations, as described in the text.

polarity observations to tightly constrain the nodal planes. Where it is not known which nodal plane is the fault plane, both possible slip vectors are shown. The clearest pattern on Fig. 10 is that there is a variation in slip vector azimuth from SW–NE on the eastern margin of the Dezful Embayment (SE of the dashed black line on Fig. 10), to SSW–NNE near the Murmuri earthquakes on the edge of the Lorestan Arc (NW of the dashed line).

The relationship between slip vector azimuth and the shape of the topography suggests two conclusions. First, although the direction of relative motion between Arabia and central Iran changes negligibly over the area covered by Fig. 10 (shown as a yellow arrow), the azimuth of the thrust slip vectors do change. This relation implies that another force also plays a role in controlling the direction of thrust motion. In addition to the forces driving the motions of the bounding plates, the other major force involved in continental deformation, and one that has been shown to control along-strike variations in thrust transport directions in other regions, is gravity acting on elevation contrasts (also known as the buoyancy force resulting from crustal thickness contrasts; e.g. England & Houseman (1988)). This force will act to move material in the down-slope direction, perpendicular to topographic contours, and is thought to be responsible for the radial thrusting directions around curved mountain ranges such the southern margin of the Tibetan Plateau and the Sulaiman Ranges of Pakistan (e.g. Copley & McKenzie 2007; Reynolds *et al.* 2015). The slip vector of the Murmuri earthquake therefore gives an indication that gravitational driving forces are important in controlling the sense of thrust motion on the margins of the Lorestan Arc and Dezful Embayment.

The second conclusion we can draw from the slip vector azimuths relates to the observation that the slip vectors are not everywhere perpendicular to the topographic contours, notably in the region of the Murmuri earthquake ('M' on Fig. 10). Here the slip vectors are rotated counter-clockwise from those further southeast, as would be expected from gravity acting on topographic contrasts. However, the slip vectors are not rotated so far as to be perpendicular to the strike of the topography. If the tractions on the base of the layer deforming in earthquakes (i.e. on the base of the sedimentary section) vary laterally, then the direct correspondence between topographic slope and thrust motion azimuth is lost (e.g. Reynolds *et al.* 2015). Such a lateral variation in tractions would be the direct result of lateral variations in the rheology of any decollement horizons within the sedimentary sequence. The lack of direct correspondence between slip vector azimuth and regional topographic slope in the Murmuri area therefore implies that there is less shear-stress being imposed on the base of the sedimentary section in the Lorestan Arc than in the Dezful Embayment to the south, which leads to an increased component of westwards motion in the Murmuri area than would be the case if the lower boundary were laterally uniform. Such a conclusion is supported by previously noted features of the mountains, including the large across-strike width and low surface gradient of the Lorestan Arc, which both suggest it is propagating over a weak lower boundary (e.g. McQuarrie 2004; Carruba *et al.* 2006). It is

unclear whether this weak lower boundary represents the Hormoz Salt or an alternative decoupling horizon. A quantitative analysis of this effect is beyond the scope of this paper, but is currently in preparation for separate publication.

9 CONCLUSIONS

The Murmuri earthquake sequence ruptured thrust faults at the boundary between the Dezful Embayment and the Lorestan Arc. The mainshock and largest aftershock both occurred on north-dipping planes, and contributed to the surface deformation observed with InSAR. The results of seismological and geodetic inversions show that the earthquake slip was dominantly or entirely contained within the thick sedimentary sequence. The relationship between the azimuth of the thrust slip vectors and the topography in the region implies that gravitational driving forces play an important role in the deformation, and that the Lorestan Arc is underlain by weaker material than the Dezful Embayment.

ACKNOWLEDGEMENTS

We thank Eric Bergman and Abdolreza Ghods for help with the hypocentral relocations, Richard Walters for providing the InSAR-derived location for the 2008 August 27 strike-slip earthquake, James Jackson for comments on the manuscript, and Jerome Neufeld for discussions on lower boundary conditions. We also thank Manuel Berberian and one anonymous reviewer for helpful comments on the manuscript. This work form part of the NERC- and ESRC-funded project 'Earthquakes Without Frontiers'. JRE is funded by the NERC projects 'COMET' and 'LiCS'.

REFERENCES

Allen, M. & Talebian, M., 2011. Structural variation along the Zagros and the nature of the Dezful Embayment, *Geol. Mag.,* **148,** 911–924.

Avouac, J.-P., Ayoub, F., Leprince, S., Konca, O. & Helmberger, D.V., 2006. The 2005, M_w 7.6 Kashmir earthquake: sub-pixel correlation of ASTER images and seismic waveforms analysis, *Earth planet. Sci. Lett.,* **249,** 514–528.

Barnhart, W.D. & Lohman, R.B., 2013. Phantom earthquakes and triggered aseismic creep: vertical partitioning of strain during earthquake sequences in Iran, *Geophys. Res. Lett.,* **20,** doi:10.1002/grl.50201.

Berberian, M., 1979. Earthquake faulting and bedding thrust associated with the Tabas-E-Golshan (Iran) earthquake of September 16, *Bull. seism. Soc. Am.,* **69,** 1861–1887.

Berberian, M., 1995. Master blind thrust faults hidden under the Zagros folds: active basement tectonics and surface morphotectonics, *Tectonophysics,* **241,** 193–224.

Berberian, M., 2014. *Earthquakes and Coseismic Surface Faulting on the Iranian Plateau*, Elsevier.

Biggs, J., Bergman, A.E., Emmerson, B., Funning, G.J., Jackson, J.A., Parsons, B.E. & Wright, T.J., 2006. Fault identification for buried strike-slip earthquakes using InSAR: The 1994 and 2004 Al Hoceima, Morocco earthquakes, *Geophys. J. Int.,* **166,** 1347–1362.

Bondar, I., Bergman, E.A., Engdahl, E.R., Kohl, B., Kung, Y. & McLaughlin, K., 2008. A hybrid multiple event location technique to obtain ground truth event locations, *Geophys. J. Int.,* **175,** 185–201.

Carruba, S., Perotti, C.R., Buonaguro, R., Calabro, R., Carpi, R. & Naini, M., 2006. Structural pattern of the Zagros fold-and-thrust belt in the Dezful Embayment (SW Iran), *Geol. Soc. Am. Spec. Pap.,* **414,** 11–32.

Casciello, E., Verges, J., Saura, E., Casini, G., Fernandez, N., Blanc, E., Homke, S. & Hunt, W., 2009. Fold patterns and multilayer rheology of the Laurestan Province, Zagros Simply Folded Belt (Iran), *J. geol. Soc. Lond.,* **166,** 947–959.

Cheloni, D. *et al.*, 2010. Coseismic and initial post-seismic slip of the 2009 Mw 6.3 L'Aquila earthquake, Italy, from GPS measurements, *Geophys. J. Int.,* **181,** 1539–1546.

Chlieh, M. *et al.*, 2007. Coseismic slip and afterslip of the great M_w 9.15 Sumatra-Andaman earthquake of 2004, *Bull. seism. Soc. Am.,* **97,** S152–S173.

Copley, A. & McKenzie, D., 2007. Models of crustal flow in the India-Asia collision zone, *Geophys. J. Int.,* **169,** 683–698.

Copley, A. & Reynolds, K., 2014. Imaging topographic growth by long-lived postseismic afterslip at Sefidabeh, east Iran, *Tectonics,* **33,** 330–345.

Copley, A., Hollingsworth, J. & Bergman, E., 2012. Constraints on fault and lithosphere rheology from the coseismic slip and postseismic afterslip of the 2006 Mw7.0 Mozambique earthquake, *J. geophys. Res.,* **117,** doi:10.1029/2011JB008580.

Delouis, B., Nocquet, J.-M. & Vallée, M., 2010. Slip distribution of the February 27, 2010 Mw = 8.8 Maule earthquake, central Chile, from static and high-rate GPS, InSAR, and broadband teleseismic data, *Geophys. Res. Lett.,* **37,** doi:10.1029/2010GL043899.

Elliott, J., Copley, A., Holley, R., Scharer, K. & Parsons, B., 2013. The 2011 Mw 7.1 Van (Eastern Turkey) earthquake, *J. geophys. Res.,* **118,** 1619–1637.

Elliott, J. *et al.*, in press. The 2013 Mw 6.2 Khaki-Shonbe (Iran) earthquake: insights into seismic and aseismic shortening of the Zagros sedimentary cover, *Earth and Space Science,* in press.

Elliott, J.R., Biggs, J., Parsons, B. & Wright, T.J., 2008. InSAR slip rate determination on the Altyn Tagh Fault, N. Tibet, in the presence of topographically correlated atmospheric delays, *Geophys. Res. Lett.,* **35,** doi:10.1029/2008GL033659.

England, P. & Houseman, G., 1988. The mechanics of the Tibetan plateau, *Phil. Trans. R. Soc. Lond.,* A, **326,** 301–320.

Freymueller, J., King, N.E. & Segall, P., 1994. The co-seismic slip distribution of the Landers earthquake, *J. geophys. Res.,* **84,** 646–659.

Geological Survey of Iran 1973. Dehluran quadrangle map.

Hessami, K., Koyi, H. & Talbot, C., 2001. The significance of strike-slip faulting in the basement of the Zagros fold and thrust belt, *Journal of petroleum Geology,* **24,** 5–28.

Jackson, J., Priestley, K., Allen, M. & Berberian, M., 2002. Active tectonics of the South Caspian Basin, *Geophys. J. Int.,* **148,** 214–245.

Jackson, J.A.M. & Kenzie, D., 1984. Active tectonics of the Alpine-Himalayan Belt between western Turkey and Pakistan, *Geophys. J. R. astr. Soc.,* **77,** 185–264.

Ji, C., Wald, D.J. & Helmberger, D.V., 2002. Source description of the 1999 Hector Mine, California, earthquake, Part 1: Wavelet domain inversion theory and resolution analysis, *Bull. seism. Soc. Am.,* **92,** 1192–1207.

Ji, C., Helmberger, D.V., Wald, D.J. & Ma, K-F., 2003. Slip history and dynamic implications of the 1999 Chi-Chi, Taiwan, earthquake, *J. geophys. Res.,* **108,** doi:10.1029/2002JB001764.

Johanson, I.A. & Burgmann, R., 2010. Coseismic and postseismic slip from the 2003 San Simeon earthquake and their effects on backthrust slip and the 2004 Parkfield earthquake, *J. geophys. Res.,* **115,** doi:10.1029/2009JB006599.

Jonsson, S., Zebker, H., Segall, P. & Amelung, F., 2002. Fault slip distribution of the 1999 Mw7.1 Hector Mine, California, earthquake, estimated from satellite radar and GPS measurements, *Bull. Seism. Soc. Am.,* **92,** 1377–1389.

Jordan, T.H. & Sverdrup, K.A., 1981. Teleseismic location techniques and their application to earthquake clusters in the south-central Pacific, *Bull. seism. Soc. Am.,* **71,** 1105–1130.

Konca, O. *et al.*, 2008. Partial rupture of a locked patch of the Sumatra megathrust during the 2007 earthquake sequence, *Nature,* **456,** 631–635.

Konca, O., Leprince, S., J-P., Avouac & Helmberger, D.V., 2010. Rupture process of the 1999 Mw 7.1 Duzce earthquake from joint analysis of SPOT, GPS, InSAR, strong-motion, and teleseismic data: a supershear rupture with variable rupture velocity, *Bull. seism. Soc. Am.,* **100,** 267–288.

Lohman, R.B. & Simons, M., 2005. Locations of selected small earthquakes in the Zagros mountains, *Geochem. Geophys. Geosyst.,* **6,** doi:10.1029/2004GC000849.

McCaffrey, R. & Abers, G., 1988. Syn3: a program for inversion of teleseismic body waveforms on microcomputers, in *Air Force Geophysical Laboratory Technical Report,* number AFGL-TR-88-0099. Hanscomb Air Force Base, MA.

McCaffrey, R., Abers, G. & Zwick, P., 1991. Inversion of teleseismic body waves, in *IASPEI Software Library,* volume 3, chapter 3.

Morris, P., 1977. Basement structure as suggested by aeromagnetic surveys in SW Iran, in *The 2nd Geological Symposium of Iran, Proceedings,* Tehran, 1977. Iran. Pet. Inst.

Motagh, M., Bahroudi, A., Haghighi, M.H., Samsonov, S., Fielding, E. & Wetzel, H.-U., 2015. The 18 August 2014 Mw 6.2 Momori, Iran, earthquake: a thin-skinned faulting in the Zagros mountain inferred from InSAR measurements, *Seismo. Res. Lett.,* in press.

Nabelek, J., 1984. Determination of earthquake source parameters from inversion of bady waves. *PhD thesis,* MIT, Cambridge, MA.

Nippress, S., Heyburn, R. & Walters, R., 2014. Relocation of the 2008 and 2012 earthquake sequences on the Zagros Foredeep fault (SE Iran/Iraq border), *AGU Fall meeting Abstracts,* pages T41C–4640.

Nissen, E., Yamini-Fard, F., Tatar, M., Gholamzadeh, A., Bergman, E., Elliott, J.R., Jackson, J.A. & Parsons, B., 2010. The vertical separation of mainshock rupture and microseismicity at Qeshm island in the Zagros fold-and-thrust belt, Iran, *Earth planet. Sci. Lett.,* **296,** 181–194.

Nissen, E., Tatar, M., Jackson, J.A. & Allen, M.B., 2011. New views on earthquake faulting in the Zagros fold-and-thrust belt of Iran, *Geophys. J. Int.,* **186,** 928–944.

Nissen, E., Jackson, J., Jahani, S. & Tatar, M., 2014. Zagros 'phantom earthquakes' reassessed – The interplay of seismicity and deep salt flow in the Simply Folded Belt? *J. geophys. Res.,* **119,** 3561–3583.

Penney, C., Copley, A. & Oveisi, B., 2015. Subduction tractions and vertical axis rotations in the Zagros-Makran transition zone, SE Iran: the 11 May 2013 Mw 6.1 Minab earthquake, *Geophys. J. Int.,* **202,** 1122–1136.

Quarrie, N.M., 2004. Crustal scale geometry of the Zagros fold-thrust belt, Iran, *J. Struct. Geol.,* **26,** 519–535.

Reynolds, K., Copley, A. & Hussain, E., 2015. Evolution and dynamics of a fold-thrust belt: the Sulaiman Range of Pakistan, *Geophys. J. Int.,* in press.

Roustaei, M. *et al.*, 2010. The 2006 March 25 Fin earthquakes (Iran)-insights into the vertical extents of faulting in the Zagros Simply Folded Belt, *Geophys. J. Int.,* **181,** 1275–1291.

Scholz, C., 1982. Scaling laws for large earthquakes: Consequence for physical models, *Bull. seism. Soc. Am.,* **72,** 1–14.

Scholz, C.H., Aviles, C. & Wesnousky, S., 1986. Scaling differences between large intraplate and interplate earthquakes, *Bull. seism. Soc. Am.,* **76,** 65–70.

Talebian, M. & Jackson, J., 2004. A reappraisal of earthquake focal mechanisms and active shortening in the Zagros mountains of Iran, *Geophys. J. Int.,* **156,** 506–526.

Taymaz, T., Jackson, J. D. M & Kenzie, 1991. Active tectonics of the north and central Aegean Sea, *Geophys. J. Int.,* **106,** 433–490.

Wald, D.J., Heaton, T.H. & Hudnut, K.W., 1996. The slip history of the 1994 Northridge, California, earthquake determined from strong-motion, teleseismic, GPS, and leveling data, *Bull. seism. Soc. Am.,* **86,** 49–70.

Walpersdorf, A. *et al.*, 2006. Difference in the GPS deformation pattern of North and Central Zagros (Iran), *Geophys. J. Int.,* **167,** 1077–1088.

Wright, T.J., Lu, Z. & Wicks, C., 2004. Constraining the slip distribution and fault geometry of the Mw 7.9, 3 November 2002, Denali Fault earthquake with interferometric synthetic aperture radar and global positioning system data, *Bull. seism. Soc. Am.,* **94,** S175–S189.

Zwick, P., McCaffrey, R. & Abers, C., 1994. Mt5 program in *IASPEI Software Library,* number 4. 1994.

APPENDIX A: FOCAL MECHANISMS OF THE MURMURI AFTERSHOCKS

Figs A1–A5 show our waveform-modelling solutions of the Murmuri aftershocks, produced using the waveform-modelling methods described in the text. Lines and symbols have the same meanings as for Fig. 2.

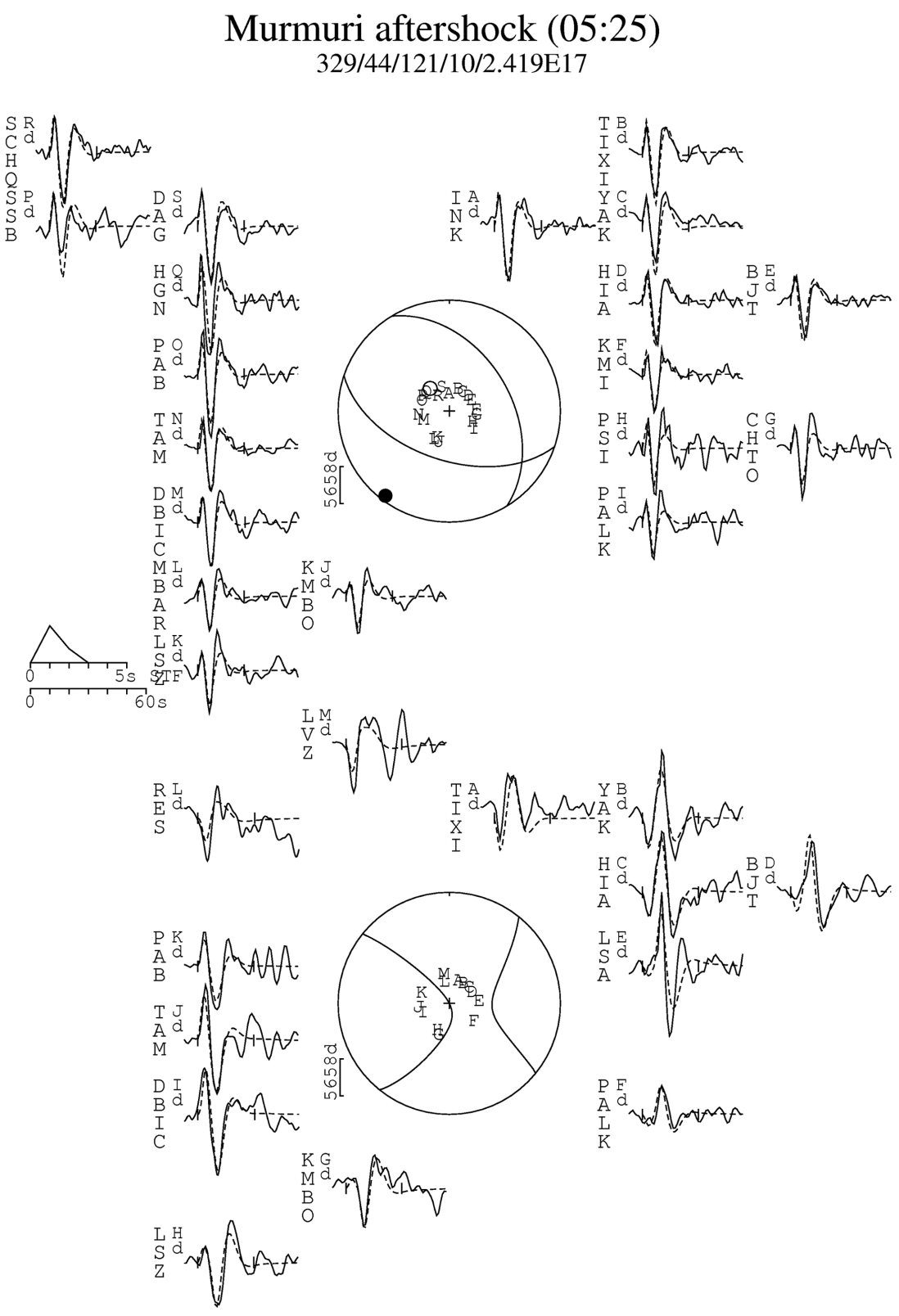

Figure A1. Mechanism of the Murmuri aftershock that occurred at 05:25 on 2014 August 18.

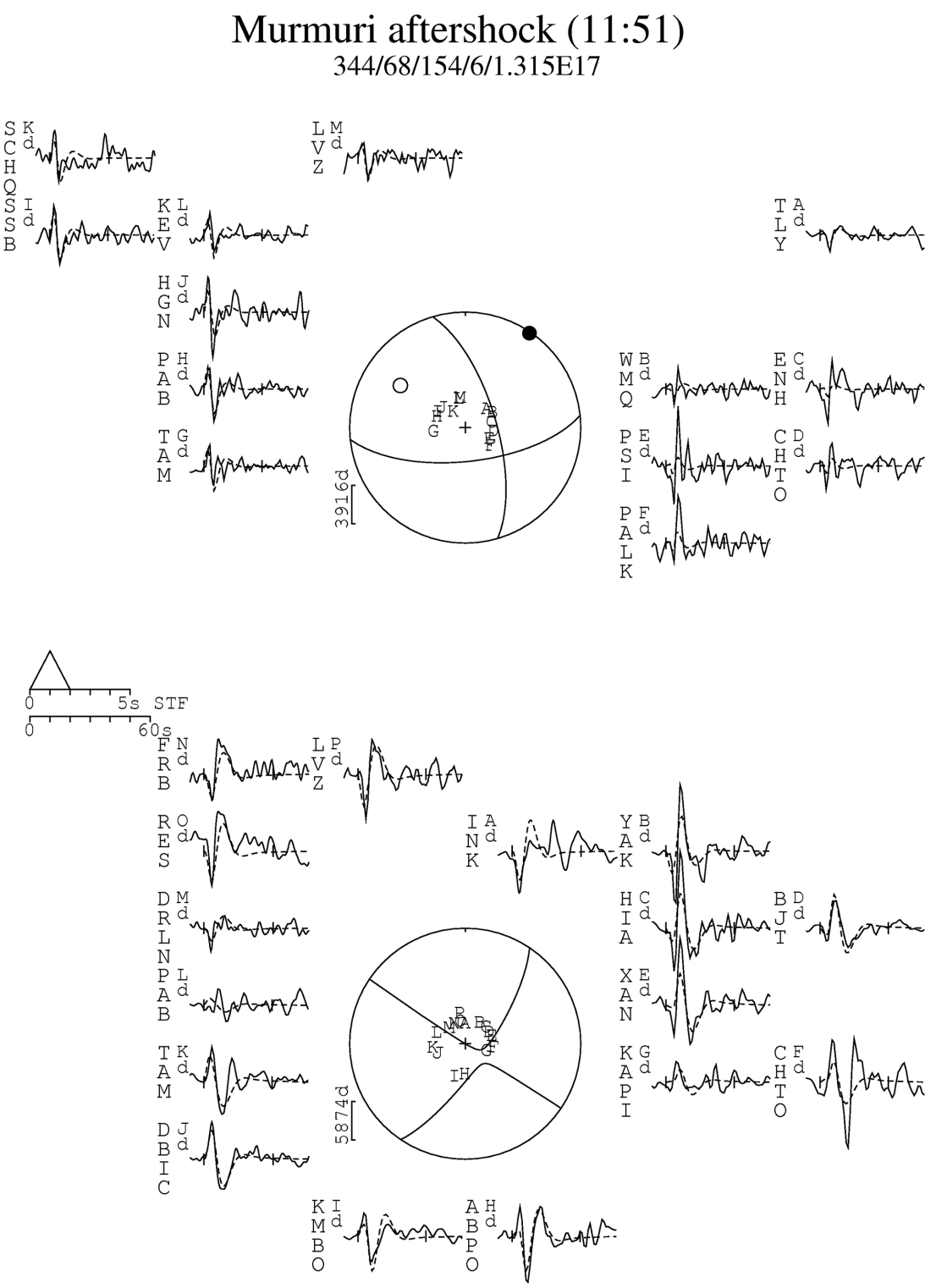

Figure A2. Mechanism of the Murmuri aftershock that occurred at 11:51 on 2014 August 18.

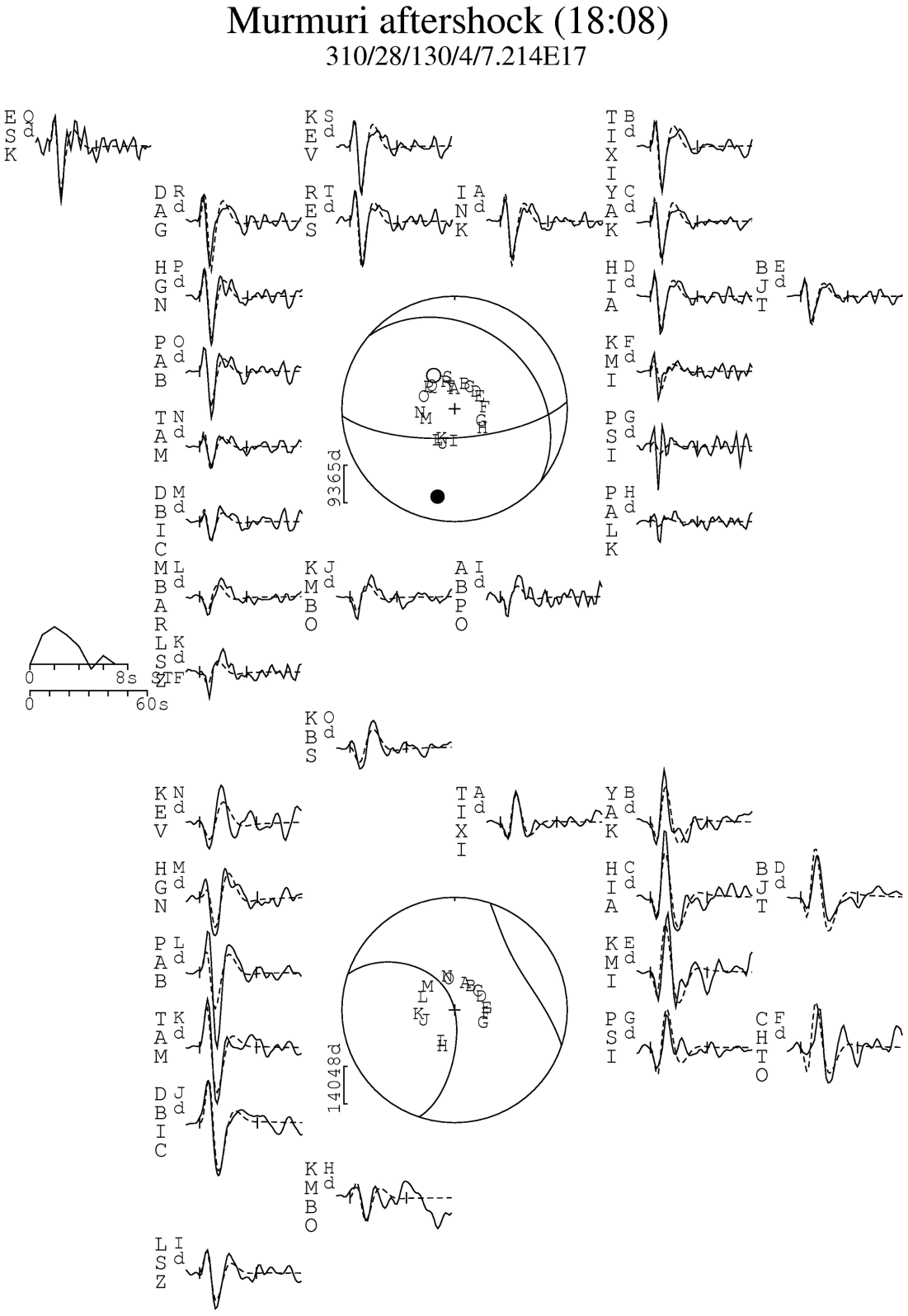

Figure A3. Mechanism of the Murmuri aftershock that occurred at 18:08 on 2014 August 18.

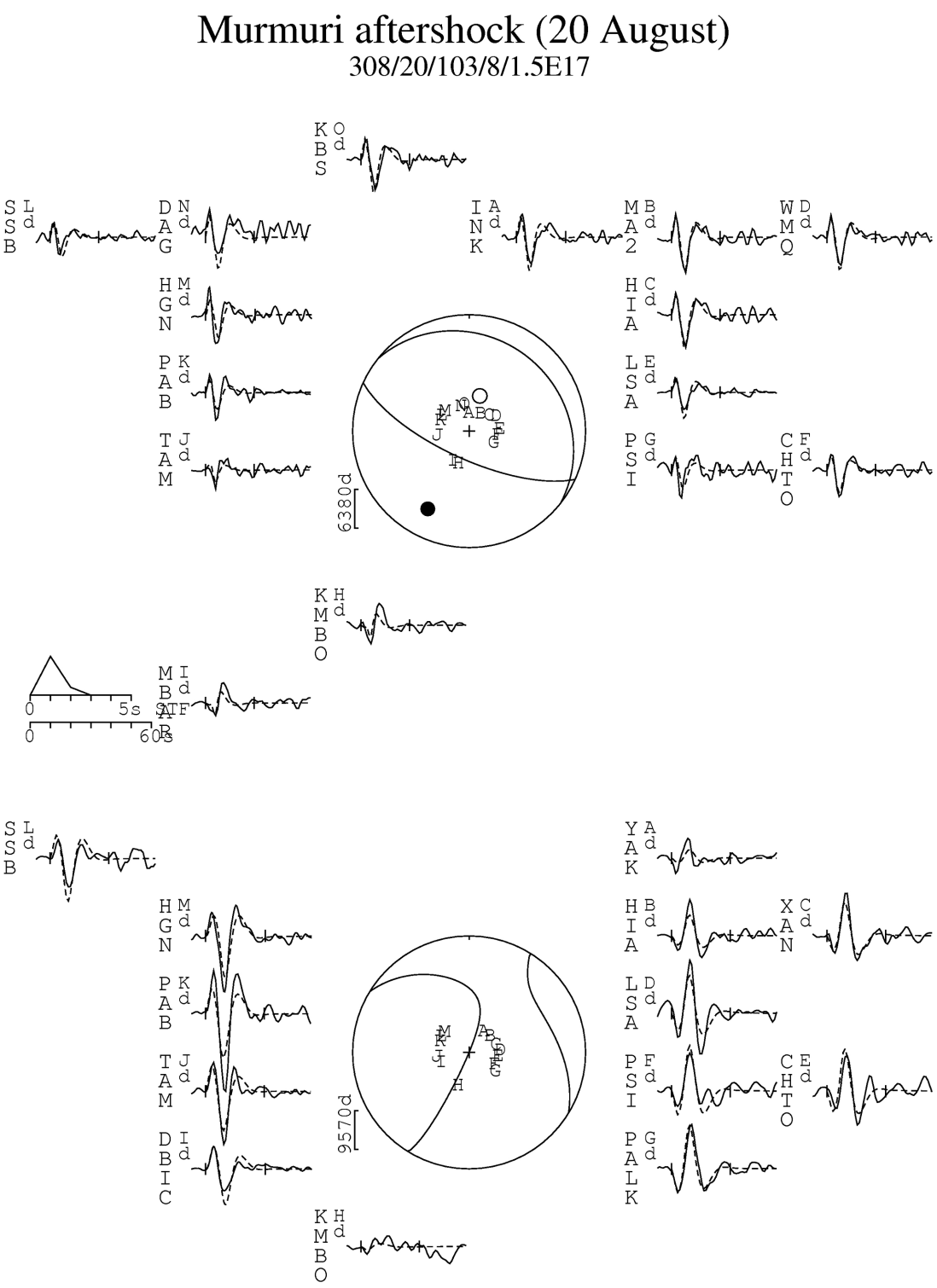

Figure A4. Mechanism of the Murmuri aftershock that occurred on 2014 August 20.

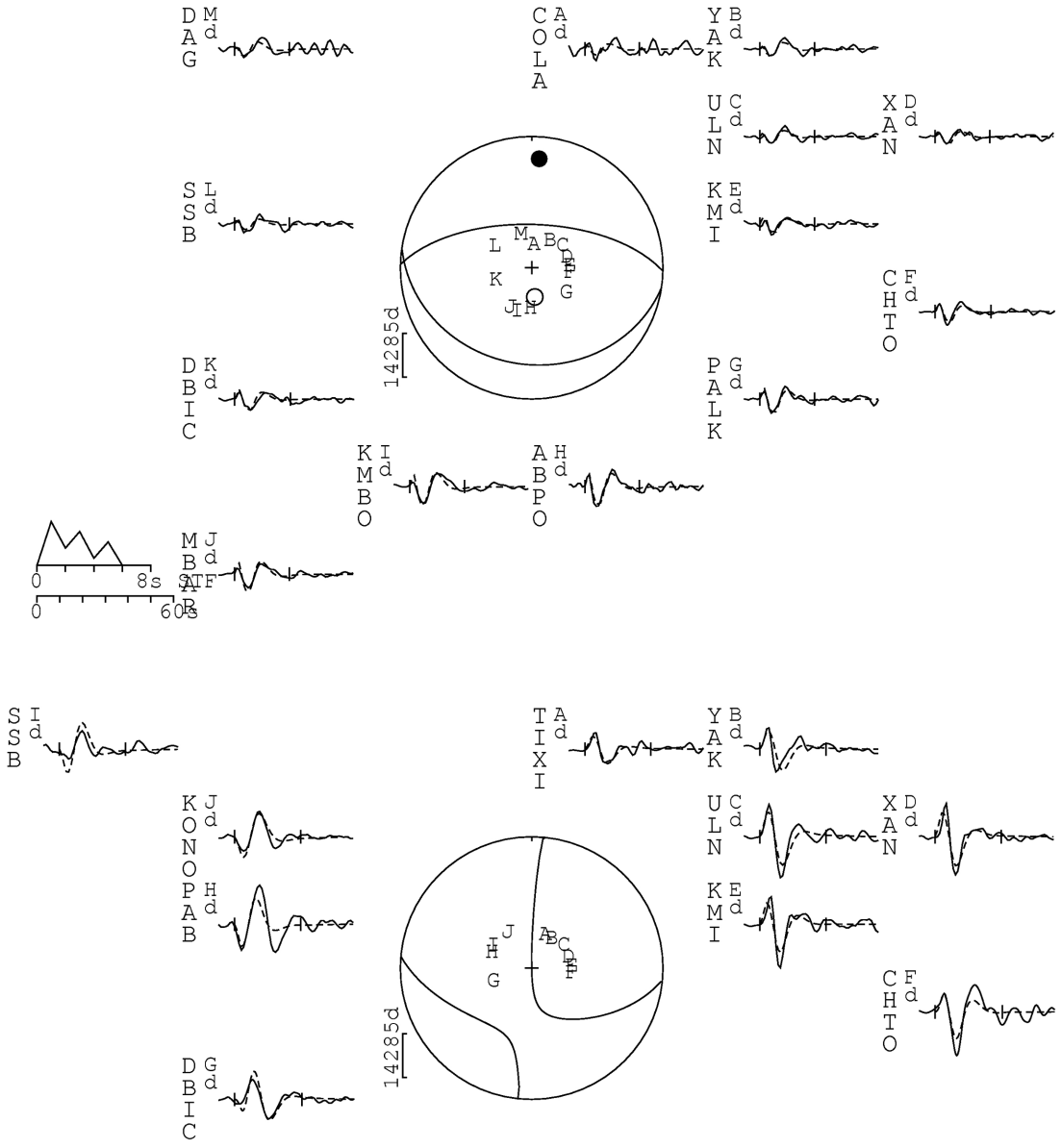

Figure A5. Mechanism of the Murmuri aftershock that occurred on 2014 October 15.

APPENDIX B: ADDITIONAL GEODETIC INVERSION RESULTS

Fig. B1 shows an inversion of the InSAR displacements using uniform-slip planes for a fault configuration in which the northern faults dip to the south and the southern fault dips to the north. Fig. B2 shows relationship between misfit and roughness for the distributed slip inversions. Figs B3 and B4 show examples of rougher and smoother solutions than the one shown in the main paper.

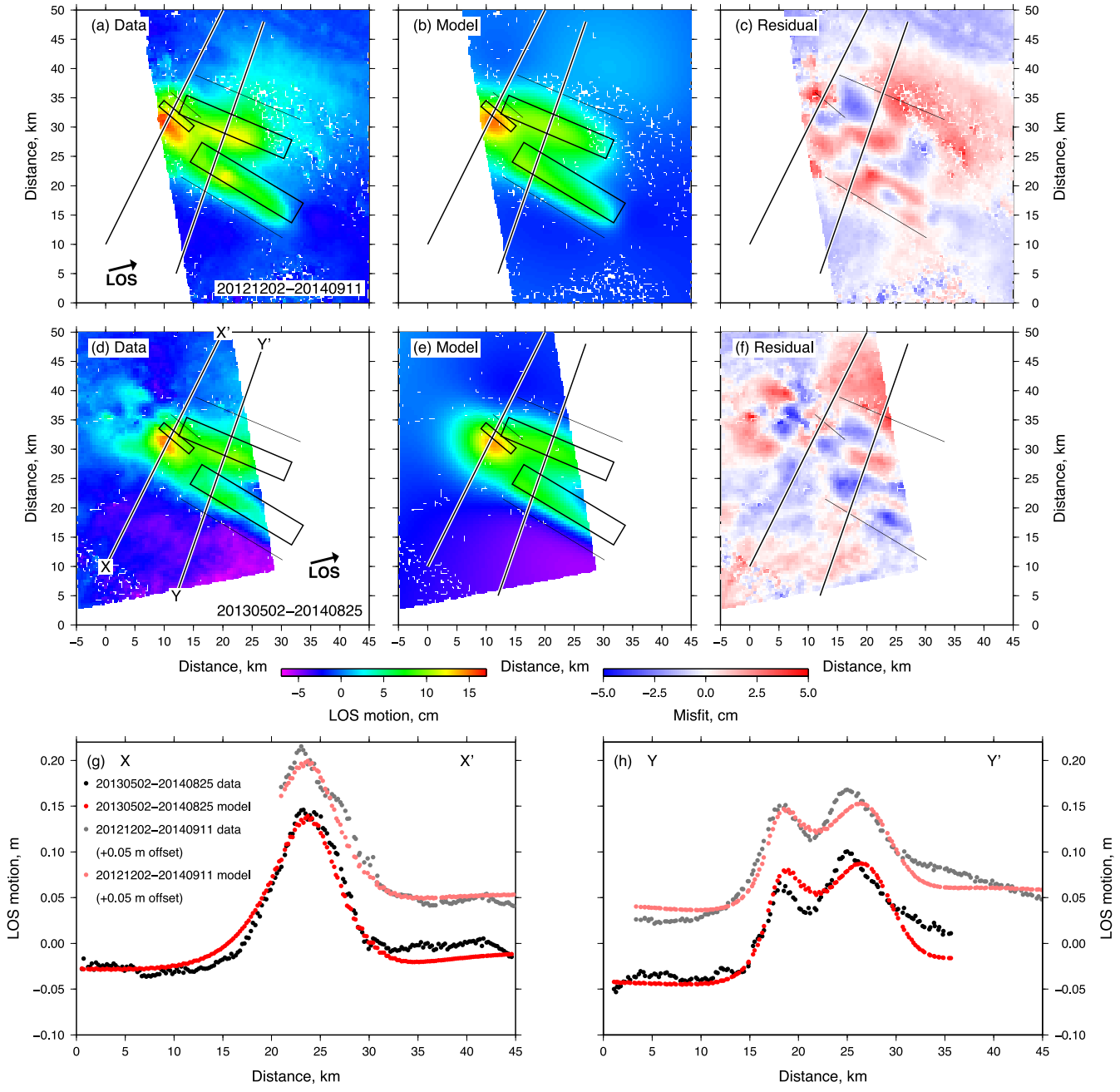

Figure B1. Data (a,d), model predictions (b,e) and residuals (c,f) for a model of the faulting in which the northern faults dip to the south, and the southern fault dips to the north. Black rectangles show the locations of the fault planes. The associated black lines show the surface projection of the fault planes, projected updip. (g,h) Profiles through the interferograms and the models along the lines X–X' and Y–Y' labelled on (d). The points relating to the 20121202–20140911 interferogram have been offset by 0.05 m for clarity.

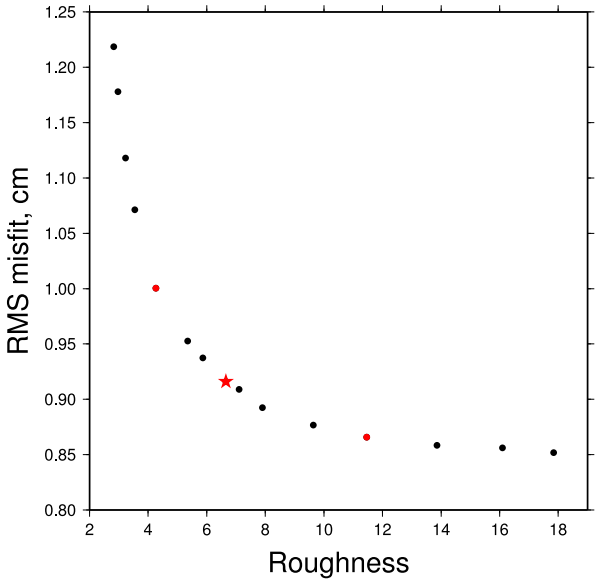

Figure B2. Relationship between model roughness and misfit in the inversions for the distribution of slip on the Murmuri fault planes. The red star shows the model in Fig. 8 in the main paper. The red circles show the rougher and smoother models shown in Figs B3 and B4.

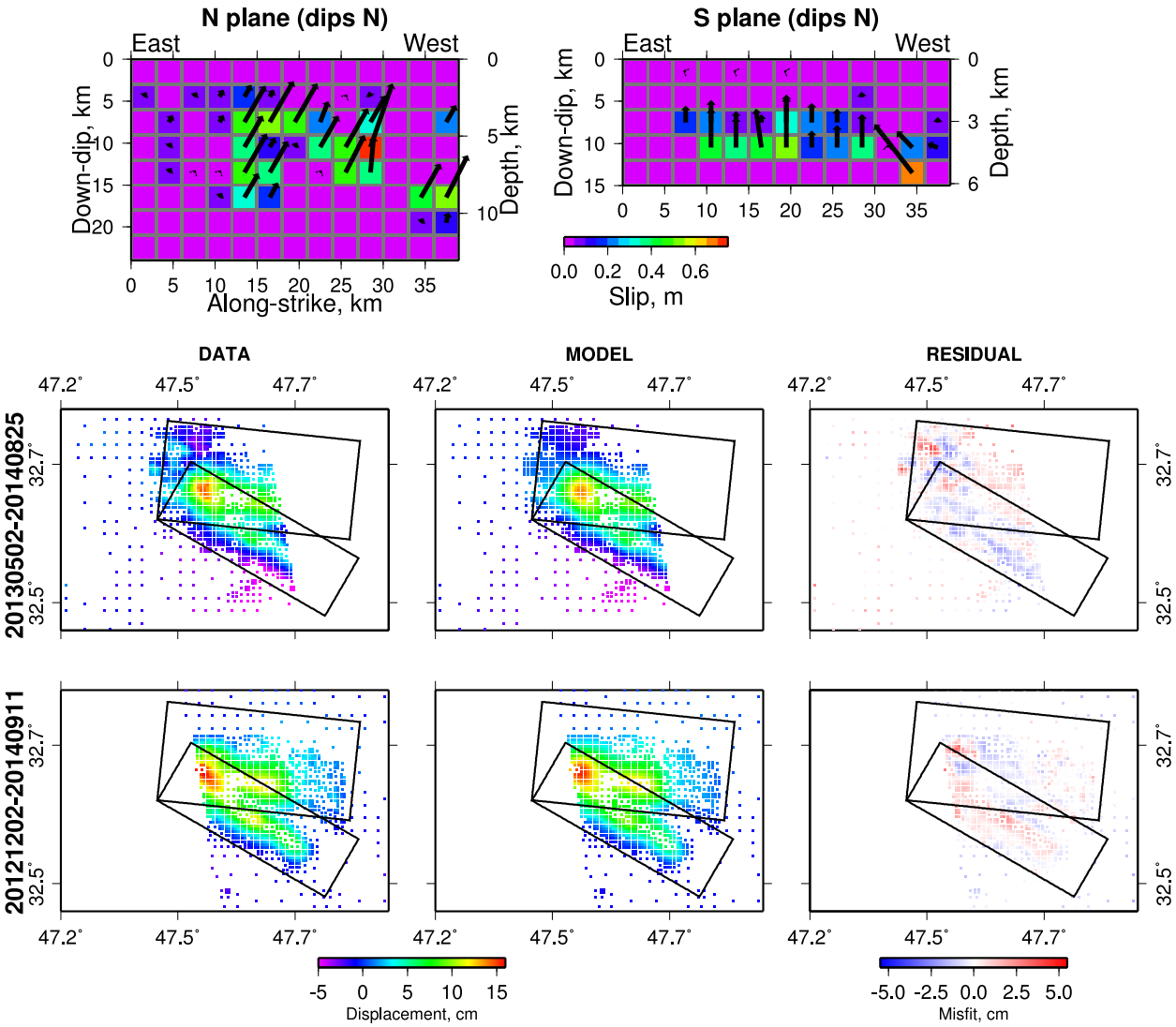

Figure B3. As Fig. 8 in the main paper, but for a rougher model (shown by the right-hand red circle in Fig. 8).

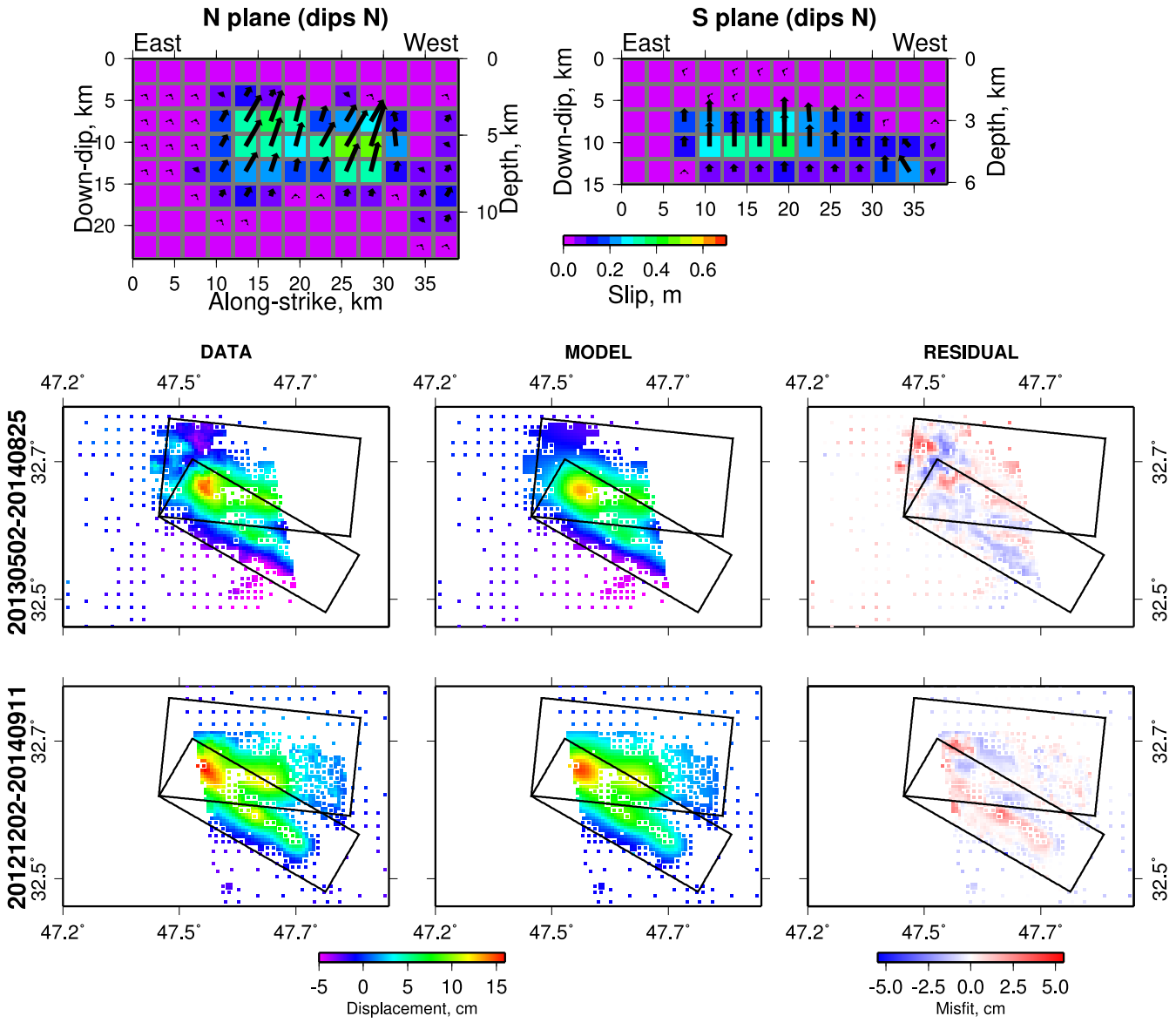

Figure B4. As Fig. 8 in the main paper, but for a smoother model (shown by the left-hand red circle in Fig. 8).

APPENDIX C: GEODETIC MODELS OF THE 15 OCTOBER AFTERSHOCK

Figs C1 and C2 show geodetic models for the aftershock that occurred on 2014 October 15.

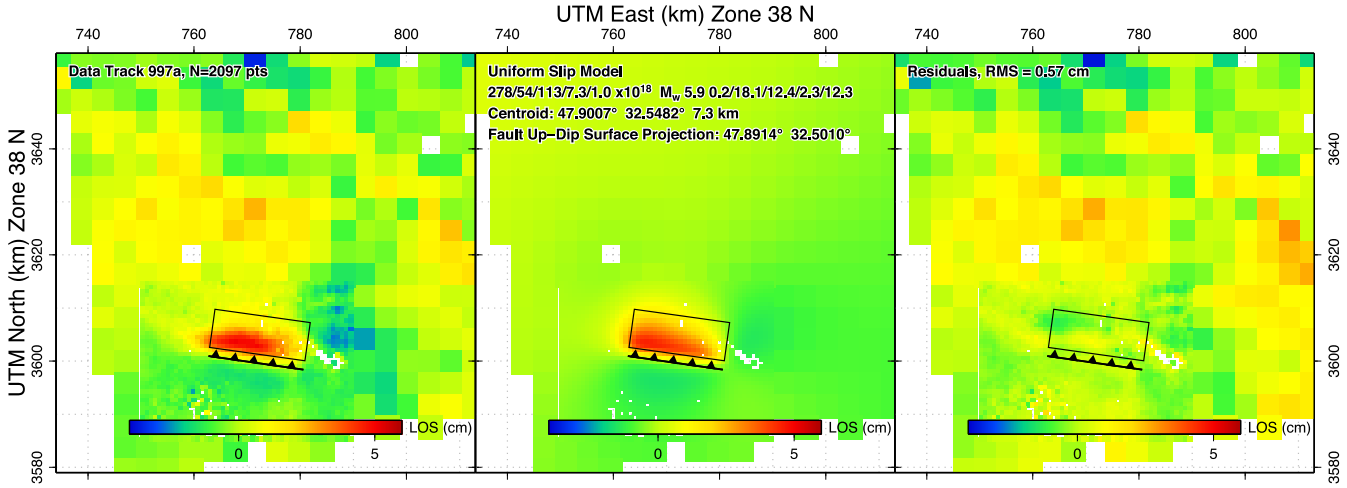

Figure C1. The left panel shows the signal of the October 15 aftershock in a Radarsat interferogram covering 2014 September 11 to 2014 October 29, which has been down-sampled for modelling purposes using a Quadtree algorithm (see Jonsson *et al.* (2002) and Wright *et al.* (2004) for detailed descriptions of this method). The centre panel shows a model prediction, and the right panel the residuals. On the centre panel the second line of text gives the fault parameters in the format strike/dip/rake/centroid depth (km)/Mo/Mw/slip (m)/length (km)/bottom depth (km)/top depth (km)/downdip width (km). The rectangle shows the plan view of the fault plane, and the barbed line shows the surface intersection of the updip projection of the fault.

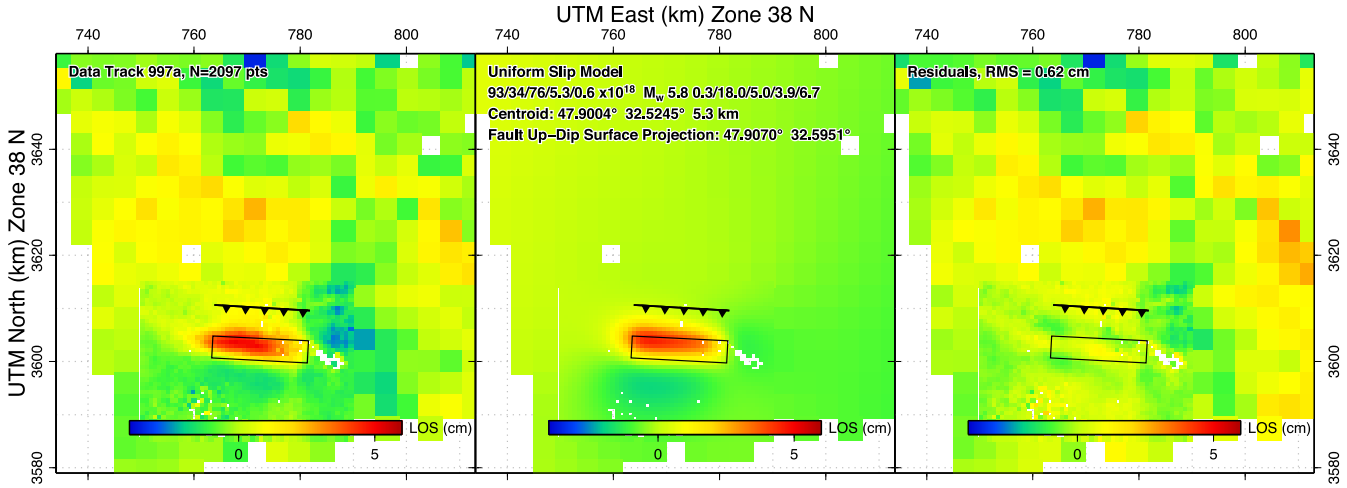

Figure C2. As Fig. C1, but for a south-dipping fault plane.